

# Chapter 10

## Compact Solar-pumped Lasers

**Hiroshi Ito, Kazuo Hasegawa, Shintaro Mizuno,  
Yasuhiko Takeda and Tomoyoshi Motohiro**

### 10.1. Introduction

#### 10.1.1. Solar-pumped Lasers and Their Possible Applications

A solar-pumped (or sun-pumped) laser (SPL) can be deemed as a variant of a conventional flash-lamp pumped laser. In SPLs, natural sunlight is used instead of flash-lamps for pumping the laser medium. Getting rid of electricity-consuming flash-lamps, SPLs are essentially renewable energy devices that convert incoherent sunlight with a wide spread of spectrum and low areal density into a monochromatic coherent laser beam with extremely high energy flux density. SPLs can be used to transmit the collected solar energy as laser beams across large distances wirelessly or via optical fibers. Some possible examples include power transmission between an orbiting space solar power station and the ground [1-5], power transmission between a lunar lander and a lunar rover exploring deep into permanently shadowed craters for frozen water [6, 7], or powering mobile objects such as drones, robots, and electric vehicles [4, 8, 9]. The transmitted laser beams can be received and converted into electricity by solar cells specially designed for the monochromatic light of the laser beams [8, 10-18]. SPLs have also been investigated to heat up materials to a higher temperature than the temperature that can be attained by simple solar concentration. A typical example includes a magnesium-based energy cycle in which solar energy is eventually stored and utilized by reduction of magnesium oxide using SPL irradiation and hydrogen production by reduction of water with magnesium [19, 20].

#### 10.1.2. Brief History of SPLs

SPLs were first reported in the 1960s [21-23], soon after the discovery of laser, that is, stimulated optical radiation in ruby [24]. Since then, more than 600 papers publicly

available papers have been published on SPLs. Iodine or iodides were the major laser mediums (LMs) intensively studied by research groups in USA (NASA and University of Florida, etc.) [25, 26], and Russia (Institute of Laser Physics, etc.) [27]. SPLs based on gas-phase dimer molecules have been actively studied by an Israeli research group (Weizmann Institute of Science) [28]. Various solid-state mediums, such as phosphate glasses [29], tellurite glass, silicate glass, fluoride glasses [22, 30-35], glass ceramics [36], borate crystals [37, 38], GdScGa-garnet crystals [39, 40], and  $\text{YAlO}_3$  [41], have also been studied for application as LMs. In one of the above-mentioned initial works on SPLs in the 1960s [23], Nd-doped yttrium aluminum garnet (Nd:YAG) single crystals were employed as LMs. Since then, Nd:YAG crystals have been the primary option for LMs [42-44]. Then, transparent Nd:YAG ceramic LMs were successfully fabricated and used widely in LMs [45, 46]. Further, transparent Cr-codoped Nd:YAG (Cr, Nd: YAG) ceramic LMs have been intensively studied by Institute for Laser Technology, Osaka and Institute of Laser Engineering, Osaka University, Japan [47]. Significant contributions have been made by Yogev et al. of Weizmann Institute of Science, Israel [48-55]. Active research on SPLs has also been ongoing in Academy of Sciences of Uzbekistan [56] and in NOVA University of Lisbon, Portugal [57-60].

### 10.1.3. Stance and Orientation of This Work

Typical sizes or diameters of solar concentrators in conventional SPL studies are in the range of 1-2 m [61, 62], such as parabolic mirrors [22, 23] and Fresnel lenses [61-64]. Some studies have employed larger solar concentrators, such as solar furnaces (mirrors) of 10 m aperture [42] and 54×48 m rectangle [65]. This trend is quite reasonable because it is necessary to harvest substantial amount of solar energy for practical solar energy utilization owing to the low areal density of sunlight (in the order of sub-kW/m<sup>2</sup>). However, for the next generation of SPLs that are more likely to be widely used for solar energy utilization (e.g., present solar cells), cost-effective and much smaller SPLs might be advantageous because they are suitable for mass production. Therefore, we explored the merits of compact SPLs and have developed prototype compact SPLs employing  $\varnothing 50.8$  mm and  $\varnothing 76.2$  mm off-axis parabolic mirrors (OAPs) for solar concentrators. An interim progress report of this research activity is provided in this chapter.

## 10.2. Background of the Concept Design

### 10.2.1. Preferable Oscillation Wavelength of SPLs

Fig. 10.1(a) schematically shows the conversion of incoherent sunlight with a wide spread of spectrum into a monochromatic coherent laser beam by an SPL. Stimulated emission of photons from an SPL at an oscillation wavelength of  $\lambda_L$  is caused by the energy of the incident sunlight of wavelength  $\lambda_i$  shorter than  $\lambda_L$  unless a means of upconversion to utilize sunlight of wavelength longer than  $\lambda_L$  is employed [66-75]. If all the photon energies of the incident sunlight of  $\lambda_i < \lambda_L$  contribute to the laser-beam output of the SPL ideally, the conversion efficiency from solar energy to laser energy  $\eta$ , that is, the ratio of the output photon energy to the total incident photon energy is given by the following expression:

$$\eta = \frac{\int_{\lambda_1}^{\lambda_2} \frac{\lambda_i}{\lambda_L} \cdot I(\lambda_i) d\lambda_i}{\int_{\lambda_1}^{\lambda_2} I(\lambda_i) d\lambda_i}, \quad (10.1)$$

where  $I(\lambda_i)$  stands for the areal power density of the incident spectral sunlight [ $\text{J}/(\text{sec} \cdot \mu\text{m} \cdot \text{m}^2)$ ]. The wavelengths  $\lambda_1$  and  $\lambda_2$  defining integral range are ideally 0 and  $\infty$ , respectively; however, in practice, they are 300 nm and 4000 nm if the main part of the intensity distribution of the solar spectrum is taken into consideration. The factor  $\lambda_i / \lambda_L$  in the integrand in the numerator in Eq. (10.1) comes from the ratio of the photon energies,  $(h \cdot c / \lambda_L) / (h \cdot c / \lambda_i)$ , representing the quantum defect caused by down-conversion. Variation of  $\eta$  as a function of  $\lambda_L$  is plotted in Fig. 10.1(b) together with the solar spectrum. Fig. 10.1(b) shows that  $\eta$  takes the optimal value in the range  $1100 \text{ nm} < \lambda_L < 1300 \text{ nm}$ . Fig. 10.1(b) also shows that  $\eta$  of this single-wavelength emission type SPL cannot exceed 0.5 even in the ideal condition [76]. If an SPL has two emission wavelengths  $\lambda_{L1}$  and  $\lambda_{L2}$  ( $\lambda_{L1} < \lambda_{L2}$ ) employing two LMs, as shown in Fig. 10.2(a),  $\eta$  can be increased over 0.6 in the wavelength regions around 864 nm for  $\lambda_{L1}$  and 1775 nm for  $\lambda_{L2}$ , as shown in Fig. 10.2(b).

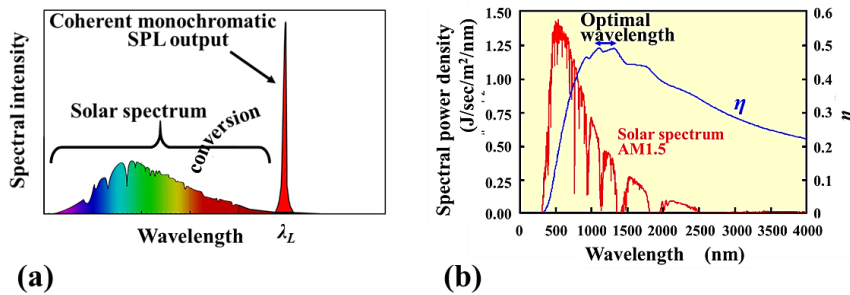


**Fig. 10.1.** (a) Function of a solar-pumped laser, (b) Variation of  $\eta$  as a function of the SPL emission wavelength  $\lambda_L$  displayed with the solar spectrum.

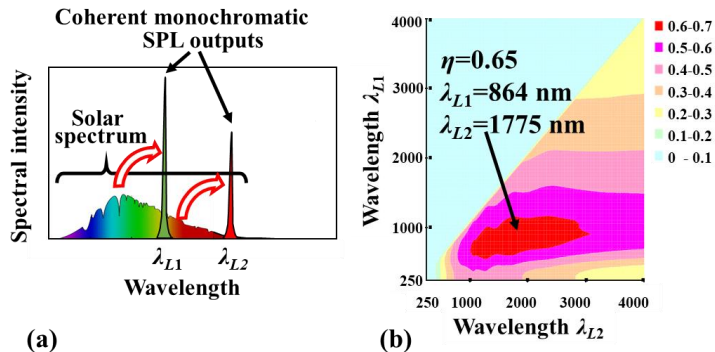


**Fig. 10.2.** (a) Function of a two-wavelength emission type SPL, and (b) Variation of  $\eta$  as a function of SPL emission wavelengths  $\lambda_{L1}$  and  $\lambda_{L2}$ .

Solar-pumped lasers utilizing emissions from Nd ions such as a Nd-doped  $Y_3Al_5O_{12}$  (Nd:YAG) crystal, described in Section 10.1, are preferable practical systems in the case of single-wavelength emission type SPL because their emission wavelength of around  $1.06 \mu\text{m}$  is near the optimal wavelength region between 1100 nm and 1300 nm shown in Fig. 10.1(b). In this case,  $\eta$  at a wavelength of  $1.06 \mu\text{m}$  is obtained as 0.48 via Eq. (10.1).

### 10.2.2. Incident Power Density Required to Oscillate SPLs

Here, we consider a case of an LM working on a four-level scheme, like the Nd:YAG transparent ceramic LMs shown in Fig. 10.3. When a four-level laser provides a constant output power under stable oscillation, the stable photon density in the LM  $N_p$  [ $1/\text{m}^3$ ] is given by the following expression:

$$N_p = \tau_c \cdot R_p - \frac{1}{\sigma(\lambda_L) \cdot c \cdot \tau}, \quad (10.2)$$

where  $R_p$  [ $1/(\text{sec} \cdot \text{m}^3)$ ] stands for the pumping efficiency, that is, the number of atoms excited per second per cubic meter;  $\sigma(\lambda_L)$  stands for the stimulated emission cross-section at the oscillation wavelength  $\lambda_L$ ;  $c$  stands for the velocity of light;  $\tau$  stands for the lifetime of spontaneous emission, which is equal to the reciprocal of the Einstein A coefficient (the rate of spontaneous emission,  $A_{32}$ ); and  $\tau_c$  [sec] stands for the cavity photon lifetime, which is expressed as

$$\tau_c = \frac{-2 \cdot L}{c \cdot \{\delta - \ln(R_1 \cdot R_2)\}}, \quad (10.3)$$

where  $L$  stands for the cavity length which is almost equal to the length of the LM,  $\delta$  stands for the round-trip resonator loss, and  $R_1$  and  $R_2$  are the reflectivity of the cavity mirrors. Eq. (10.2) is schematically visualized in Fig. 10.4.

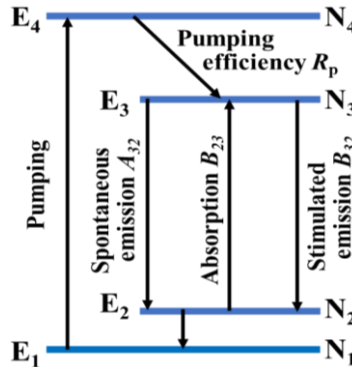
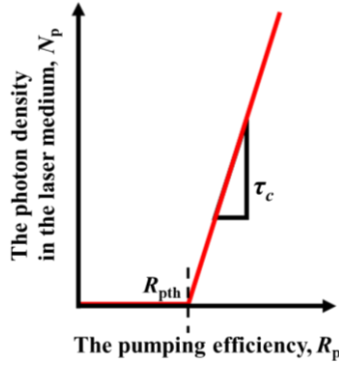


Fig. 10.3. Four level laser scheme.



**Fig. 10.4.** Stable photon density in the LM as a function of pumping efficiency.

As elucidated in Fig. 10.4, the value of  $R_p$  when  $N_p$  decreases to zero,  $R_{pth}$  is the minimum pumping efficiency, that is, the threshold pumping efficiency to cause laser oscillation. Using Eqs. (10.2) and (10.3),  $R_{pth}$  is expressed as

$$R_{pth} = -\frac{\delta - \ln(R_1 \cdot R_2)}{2\sigma(\lambda_L) \cdot \tau \cdot L} \quad (10.4)$$

Here, we consider a rod type LM of diameter  $2r$  and length  $L$  pumped by the light  $I_e$  [W/m<sup>2</sup>] of frequency  $\nu_e$  from the left mainly on the left end facet and partly on the side surface, as schematically illustrated in Fig. 10.5. The total number of photons that contribute to pumping the rod is given by

$$\frac{I_e}{h \cdot \nu_e} (\pi \cdot r^2 + 2\pi \cdot r \cdot \alpha L), \quad (10.5)$$

where  $h$  stands for the Planck constant =  $6.626 \times 10^{-34}$  J·sec. Here, the factor  $\alpha$  ( $0 \leq \alpha \leq 1$ ) is used to express effective length  $\alpha L$  of the side surface that receives photons. Dividing Eq. (10.5) by the volume of the rod,  $\pi \cdot r^2 \cdot L$ , the number of excited ions per second per volume  $R_e$  is expressed by

$$R_e = \left( \frac{I_e}{h \cdot \nu_e} \right) \cdot \left( \frac{1}{L} + \frac{2\alpha}{r} \right) \cdot \eta = \left( \frac{I_e}{h \cdot \nu_e} \right) \cdot \frac{1}{L} \cdot (1 + 2\alpha \cdot A) \cdot \eta, \quad (10.6)$$

where  $A (= L/r)$  is the aspect ratio of the rod, and  $\eta$  is the total pumping efficiency; it is expressed as follows:

$$\eta = \eta_{QD} \cdot \eta_{QE} \cdot \eta_{abs} \cdot \eta_m, \quad (10.7)$$

where  $\eta_{QD}$  stands for quantum defect representing the ratio of photon energy of the emitted laser to that of the pumping light,  $\eta_{QE}$  stands for quantum efficiency representing the ratio

of number of photons contributing the excitation of ions to the number of absorbed photons,  $\eta_{\text{abs}}$  represents the ratio of the number of absorbed photons to the number of incident photons to the rod reflected by the degree of matching of the absorption spectrum of the rod material with the sunlight spectrum,  $\eta_m$  stands for mode-matching efficiency representing the ratio of number of excited ions distributing in the laser oscillation mode and contributing to the laser oscillation to the total excited ions in the rod. Laser oscillation takes place when  $R_e$  in Eq. (10.6) exceeds  $R_{\text{Pth}}$  in Eq. (10.4). Combining Eq. (10.4) with Eq. (10.6), the threshold of the incident power density to start laser oscillation  $I_{\text{eth}}$  [W/m<sup>2</sup>] is expressed as follows:

$$I_{\text{eth}} = \left( \frac{h \cdot \nu_e}{\sigma(\lambda_L) \cdot \tau} \right) \cdot \left( \frac{\delta - \ln(R_1 \cdot R_2)}{2} \right) \cdot \left( \frac{1}{1 + 2\alpha A} \right) \cdot \left( \frac{1}{\eta_{\text{QD}} \cdot \eta_{\text{QE}} \cdot \eta_{\text{abs}} \cdot \eta_m} \right) \quad (10.8)$$

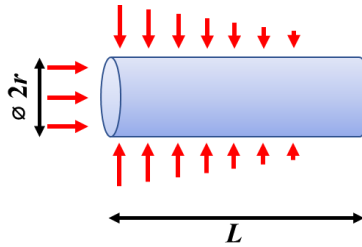


**Fig. 10.5.** A rod type LM pumped by light mainly on the left end facet and partly on the side surface.

Eq. (10.8) shows that to decrease  $I_{\text{eth}}$  for ease of laser oscillation, lower  $\nu_e$ , in other words, larger  $\lambda_e$  under the constraint of  $\lambda_e < \lambda_L$  (the lower quantum defect); larger  $\sigma(\lambda_L) \cdot \tau$ ; lower cavity loss; higher reflectivity of the cavity mirrors; larger effective aspect ratio  $\alpha A$ ; and larger  $\eta_{\text{QD}}$ ,  $\eta_{\text{QE}}$ ,  $\eta_{\text{abs}}$ , and  $\eta_m$  are preferable. It should be noted that  $L$  is not related to  $I_{\text{eth}}$  in Eq. (10.8) explicitly because both Eqs. (10.4) and (10.6) contain  $L$  in their denominators.

In a typical case of Nd:YAG laser with  $\lambda_L$  of 1064 nm,  $\lambda_e$  of 808 nm,  $\sigma(\lambda_L)$  of  $2.8 \times 10^{-19}$  cm<sup>2</sup>,  $\tau$  of 230  $\mu$ sec,  $R_1$  of 0.99,  $R_2$  of 0.95,  $\eta_{\text{QD}}$  of 0.61 (= 650 nm / 1064 nm),  $\eta_{\text{QE}}$  of 1,  $\eta_{\text{abs}}$  of 0.3,  $\eta_{\text{abs}}$  of 0.29,  $A$  of 20 (= 10 mm / 0.5 mm), and  $\alpha$  of 0.03,  $I_{\text{eth}}$  was calculated to be 5427 kW/m<sup>2</sup>. Therefore, a solar concentration ratio of more than 5500 is required for 1 Sun solar insolation of 1 kW/m<sup>2</sup> to start oscillation in this laser rod.

### 10.2.3. Preferable Shape of LMs for SPLs

The volume  $V$  and the total surface area  $S$  of the typical LM shown in Fig. 10.5 are given by

$$V = \pi \cdot r^2 \cdot L, \quad (10.9)$$

$$S = 2\pi \cdot r \cdot L + 2\pi \cdot r^2, \quad (10.10)$$

respectively. Using Eq. (10.9),  $A = L / r$ , and normalizing  $S$  by the values of  $S$  when  $A$  is 2,  $S_{A=2}$ , under the fixed  $V$ , Eq. (10.10) can be modified as

$$\frac{S}{S_{A=2}} = \frac{2^{\frac{2}{3}}}{3} \cdot A^{\frac{1}{3}} \cdot \left(1 + \frac{1}{A}\right) \quad (10.11)$$

Fig. 10.6 shows the variation of  $S/S_{A=2}$  as a function of  $A$ . Fig. 10.6 shows that the total surface area of the LM takes high values under fixed  $V$  in the left-hand side and the right-hand side of the graph. Therefore, the total number of pumping photons expressed in Eq. (10.5) also takes a large value in the small  $A$  range and in the large  $A$  range in the fixed volume. This means that thin disk-type LMs, and thin fiber-type LMs are preferable for SPL because of the low areal energy density of sunlight. The high  $A$  values in the thin disk-type LMs and thin fiber-type LMs are also advantageous for thermal dissipation, as intuitively shown by the pink arrows in Fig. 10.6. In the case of a Nd:YAG crystal, for example, the theoretical upper limit of solar energy conversion efficiency into monochromatic laser at a wavelength of  $1.06 \mu\text{m}$  is calculated to be 0.48, as described in Subsection 10.2.1. However, actual feasible conversion efficiency will be much lower [76]. Since most of the concentrated solar energy is converted to heat mainly in the LM, without rapid thermal dissipation,  $\sigma(\lambda_L) \cdot \tau$  in Eq. (10.8) decreases and an inhomogeneous temperature increase in the LM can take place. This causes degradation of the laser-beam quality because of temperature dependent refractive index, including thermal lens effect, loss of the energy conversion efficiency, and even the breakage of LMs. Therefore, the advantage of thermal dissipation in thin disk-type, and thin fiber-type LMs is of key importance. Here, it is suggested that a glass LM is promising for SPLs because it can be easily molded into thin disks and thin fibers. High solubility of rare earth elements such as Nd is another attractive property of glass LMs. Further, the suitability of glass LMs for mass production ensures low production costs, which is a key factor for wide adoption of SPLs in the society.

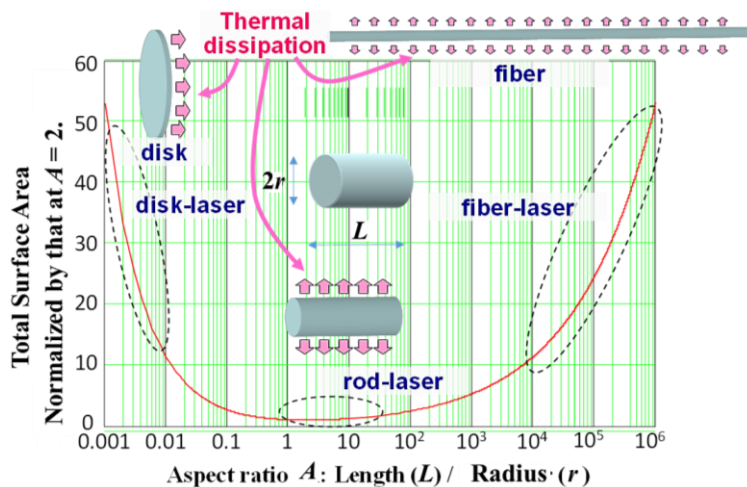


Fig. 10.6. Variation of  $S/S_{A=2}$  as a function of  $A$ .

### 10.2.4. Theoretical Limit of Solar Concentration

Suppose the Sun is a perfect blackbody of radius  $R_S$  (m) and surface temperature  $T_S$  (K), the total radiant flux power from the Sun,  $P_O$  (W), is given by

$$P_O = 4\pi \cdot R_S^2 \cdot \sigma \cdot T_S^4, \quad (10.12)$$

where  $\sigma$  stands for the Stefan-Boltzmann constant  $= 5.67 \times 10^{-8} \text{ W}/(\text{m}^2\text{K}^4)$ , and  $\sigma \cdot T_S^4$  represents the radiant flux power density at the surface of the Sun based on the Stefan-Boltzmann law. At the average radius of Earth's orbit around the Sun, that is, one astronomical unit  $A_u$  (m), the radiant flux power density  $I_O$  ( $\text{W}/\text{m}^2$ ) is called the solar constant and is given by

$$I_O = \frac{P_O}{4 \cdot \pi \cdot A_u^2} = \frac{R_S^2}{A_u^2} \cdot \sigma \cdot T_S^4 \quad (10.13)$$

$I_O$  is calculated to be  $1367 \text{ W}/\text{m}^2$ . The solar concentration ratio  $C$  is defined as the ratio of the radiant flux power density at the most concentrated location near the focal point of the solar concentrator to the radiant flux power density of sunlight at the entrance of the concentrator. Thus, the radiant flux power density at the most concentrated location near the focal point of the solar concentrator  $I'$  ( $\text{W}/\text{m}^2$ ) is given by

$$I' = C \cdot \frac{R_S^2}{A_u^2} \cdot \sigma \cdot T_S^4 = \sigma \cdot T'^4 \quad (10.14)$$

Suppose the most concentrated location near the focal point of the solar concentrator is on a perfect blackbody surface, the surface temperature  $T$  K of this blackbody is required to be lower than  $T_S$  based on the principles of thermodynamics. Then the following inequality expression can be deduced.

$$C \leq \frac{A_u^2}{R_S^2} = \frac{1}{(\sin \theta_s)^2}, \quad (10.15)$$

where  $\theta_s$  is the apparent Sun semidiameter observed from the average Earth's orbit around the Sun, as illustrated in Fig. 10.7.

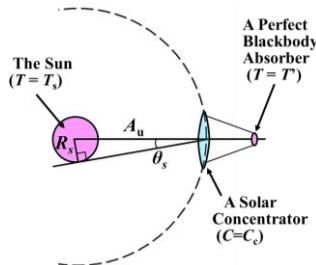


**Fig. 10.7.** Schematic geometry of the Sun, a solar concentrator on the average Earth's orbit around the Sun and a blackbody absorber near its focal point.

This is the theoretical limit of the solar concentration ratio  $C_O$  deduced from the laws of thermodynamics. The same results can be obtained from the Lagrange-Helmholtz invariant or Luminance conservation law, naturally. By substituting the values  $R_S = 6.96 \times 10^8$  m and  $A_u = 1.496 \times 10^{11}$  m into Eq. (10.15), we obtain

$$C \leq C_o = 46200 \quad (10.16)$$

### 10.2.5. Size of Images of the Sun and Concentration Ratios by Solar Concentrators

#### 10.2.5.1. Convex Lens

Fig. 10.8 illustrates the geometry of image formation by a convex lens comprised of an object, a lens, and an image of the object located graphically by means of geometrical optics [77]. The white arrow on the left side of the lens represents an object of length  $R_s$ . The distance between the foot of this white arrow and the center of the lens O is supposed to be  $A_u$ . Correspondingly, the smaller upside-down white arrow of length  $r_s$  appears on the right side of the lens as an image of the white arrow on the left side of the lens. The distance between the foot of the image and O is expressed as  $f + x$ , where  $f$  stands for the focal length of the lens. A black arrow of length  $D$ , which is equal to the radius of the lens is marked on the white arrow on the left of the lens. Correspondingly, a black arrow of length  $d$  also appears upside-down on the image of the white arrow on the right side of the lens. From the two similar triangles with a common vertex F, the following Eq. (10.17) can be obtained:

$$\frac{d}{x} = \frac{D}{f} \quad (10.17)$$

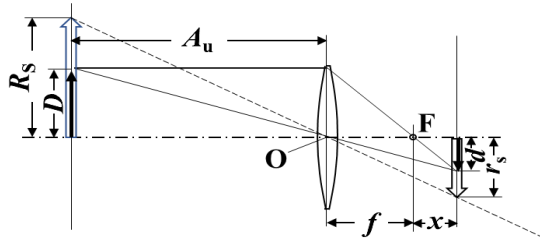


**Fig. 10.8.** Illustration of image formation by a convex lens tracing several characteristic rays.

From the other two similar triangles with common vertex O, the following Eq. (10.18) can be obtained:

$$\frac{d}{f + x} = \frac{D}{A_u} \quad (10.18)$$

From Eqs. (10.17) and (10.18),  $r_s$  is expressed as follows:

$$r_s = d \cdot \frac{R_s}{D} = \frac{R_s}{A_u} \cdot \frac{f}{1 - \frac{f}{A_u}} \cong \frac{R_s}{A_u} \cdot f \quad (10.19)$$

In Eq. (10.19), the denominator was partly approximated using the relation  $f/A_u \ll 1$ . In a specific case of  $f = 50.8$  mm, the radius of the image of the Sun is obtained to be 0.236 mm. The concentration ratio can be expressed as follows:

$$\frac{\pi D^2}{\pi r_s^2} = \frac{D^2}{\left( \frac{R_s}{A_u} \cdot \frac{f}{1 - \frac{f}{A_u}} \right)^2} \cong \left( \frac{A_u}{R_s} \right)^2 \cdot \left( \frac{D}{f} \right)^2 \quad (10.20)$$

As indicated in Eqs. (10.15) and (10.16),  $(A_u/R_s)^2$  is the theoretical upper limit of solar concentration ratio. In a typical case of  $f = 50.8$  mm and  $2D = 50.8$  mm, the concentration ratio is 25 % of the theoretical upper limit. In practical aplanatic lenses that are nearly free of coma and spherical aberration,  $D/f$  does not exceed 0.7, usually. Therefore, solar concentration ratios are usually less than 50 % of the theoretical upper limit. In practice, a lens transmittance loss of between 0.25 and 0.9 ensures that solar concentration ratios are between 12.5 % and 45 % of the theoretical upper limit.

### 10.2.5.2. Parabolic Concave Mirror

Fig. 10.9 illustrates the geometry of image formation by a parabolic concave mirror in the same manner as Fig. 10.8. Through similar geometrical consideration, the same relation as Eq. (10.18) is obtained. The equation corresponding to Eq. (10.17) can be obtained as Eq. (10.21).

$$\frac{d}{x} = \frac{D}{f - \frac{D^2}{4f}} \quad (10.21)$$

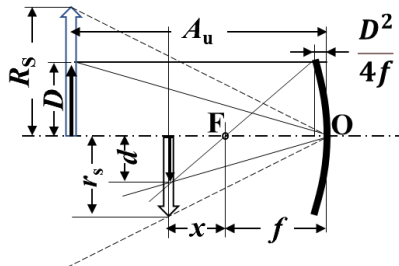


**Fig. 10.9.** Illustration of image formation by a parabolic concave mirror tracing several characteristic rays.

Here, the factor  $D^2/4f$  in the right-hand denominator corresponds to the displacement of the mirror surface to the left at its edge. From Eqs. (10.18) and (10.21),  $r_s$  is expressed as follows:

$$r_s = \frac{R_s}{D} \cdot d = \frac{R_s}{A_u} \cdot \frac{f}{1 - \frac{1}{A_u} \cdot \left( f - \frac{D^2}{4f} \right)} \cong \frac{R_s}{A_u} \cdot f \quad (10.22)$$

In Eq. (10.22), the denominator was partly approximated using the relation  $f/A_u \ll 1$ . In a typical case of  $f = 50.8$  mm, the radius of the image of the Sun is obtained to be 0.236 mm. The concentration ratio can be eventually expressed in the same manner as Eq. (10.20):

$$\frac{\pi D^2}{\pi r_s^2} = \left( \frac{A_u}{R_s} \right)^2 \cdot \frac{D^2}{\left[ \frac{f}{1 - \frac{1}{A_u} \cdot \left( f - \frac{D^2}{4f} \right)} \right]^2} \cong \left( \frac{A_u}{R_s} \right)^2 \cdot \left( \frac{D}{f} \right)^2 \quad (10.23)$$

Thus, for a typical case of  $f = 50.8$  mm, and  $2D = 50.8$  mm, the concentration ratio is 25 % of the theoretical upper limit.

### 10.2.6. Merits of Miniaturization of SPLs

Fig. 10.10 shows photos of Odeillo solar furnace at the Process, Materials and Solar Energy (PROMES)-CNRS laboratory. It is one of the largest solar furnaces in the world, situated in the Pyrenees mountain range in the south of France, and has been used as a solar concentrator for an SPL [65]. Its height, width, and focal length are 54 m, 48 m, and 18 m, respectively. With the aid of 63 flat plate heliostats, it attains a temperature of 3500 °C and concentrates 1 MW at the focus. It should be noted that the expressions for the solar concentration ratio of a convex lens (Eq. (10.20)) and of a parabolic mirror (Eq. (10.23)) do not contain the absolute sizes of the solar concentrator, such as the focal length  $f$  and the diameter  $2D$ , but contain the ratio  $D/f$ . Therefore, the same radiant flux power density as the Odeillo solar furnace can be attained by a much more compact solar concentrator, for example, of height, width, and focal length = 5.4 cm, 4.8 cm, and 1.8 cm, respectively, although the total amount of the concentrated solar power would be much less than 1 MW.

As a typical example of a conventional SPL, a 1.4×1.05 m Fresnel lens with a focal length of 1.2 m and a Cr-codoped Nd:YAG ceramic LM was used for an SPL system and 18.7 W laser output was obtained [64]. The corresponding NA was 0.4-0.5. For simplicity, let us consider an SPL system composed of a  $\varnothing 1.37$  m lens with a focal length of 1.2 m (NA = 0.5) and a  $\varnothing 10 \times 100$  mm cylindrical Cr-codoped Nd:YAG LM, as shown in Fig. 10.11(a). The sunlight-receiving area  $(1.37/2)^2 \times \pi$  is equal to 1.4×1.05 m<sup>2</sup>. Most of

the focused sunlight is introduced into the rod because the size of the image of the Sun is calculated to be approximately  $\varnothing 8.2$  mm according to Eq. (10.19). It is duly conjectured that this SPL can also oscillate and yield a similar amount of laser output as in reference [64]. Then, let us consider a miniaturized SPL system composed of  $\varnothing 76.2$  mm with a focal length of 66 mm ( $NA = 0.5$ ) and a cylindrical LM of  $\varnothing 1 \times 10$  mm as shown in Fig. 10.11(b). Most of the focused sunlight is introduced into the rod because the size of the image of the Sun is calculated to be approximately  $\varnothing 0.62$  mm according to Eq. (10.19). This miniaturized SPL will be able to oscillate in natural sunlight because the focused radiant flux power densities are the same between the  $\varnothing 1.37$  m lens and the miniaturized  $\varnothing 76.2$  mm system because Eqs. (10.20) and (10.23) do not relate to the absolute size  $D$  or  $f$  but only  $D/f$ . However, the absolute value of the laser output power is approximately  $1/323$  in proportion to the ratio of the sunlight-receiving areas. Therefore, an array of 324 miniaturized SPLs will make more laser output power than the system of  $\varnothing 1.37$  m lens. Here, the total volume of the ceramics LMs in this array is  $810\pi$  mm<sup>3</sup> ( $2.5\pi$  mm<sup>3</sup>  $\times$  324), which is much less than the  $2500\pi$  mm<sup>3</sup> ( $25\pi \times 100$ ) in the  $\varnothing 1.37$  m lens system. In addition to the advantage of having less volume, the  $\varnothing 1 \times 10$  mm Cr-codoped Nd:YAG LMs are easier to fabricate and more suitable for mass production compared to the  $\varnothing 10 \times 100$  mm LM. The  $\varnothing 1 \times 10$  mm micro laser rod is also advantageous in comparison with the conventional size laser rod, such as the one of  $\varnothing 10 \times 100$  mm, from the view point of rapid thermal dissipation owing to reasons explained earlier. As for the solar concentrator, compact solar concentrators together with the corresponding solar-tracking systems are cost-effective because they have already been mass produced and used in various commercial applications, such as the solar lighting system “Himawari” with a solar-tracking system by La Foret Engineering Company (Japan) [78]. This is in contrast to the large systems, such as  $\varnothing 1.37$  m lens, which are still in the made-to-order stage.

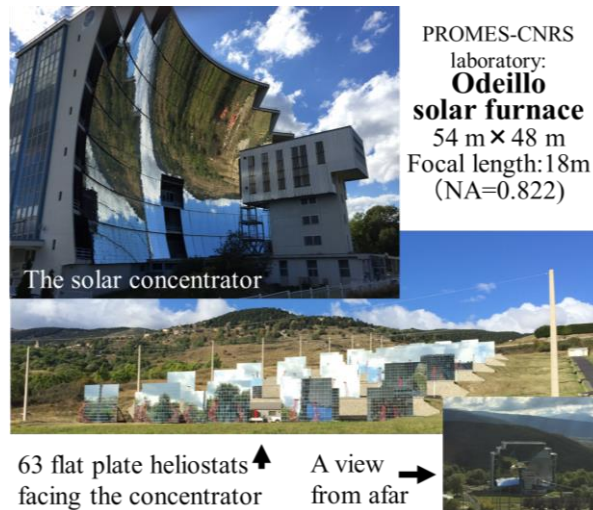


**Fig. 10.10.** Odeillo solar furnace of the Process, Materials and Solar Energy (PROMES)-CNRS laboratory in France (photograph taken on October 9<sup>th</sup>, 2018).

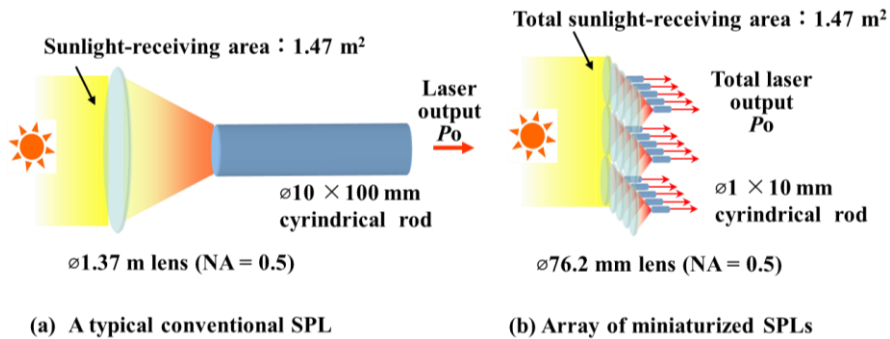


**Fig. 10.11.** Concept of miniaturization of SPLs keeping laser output power unchanged.

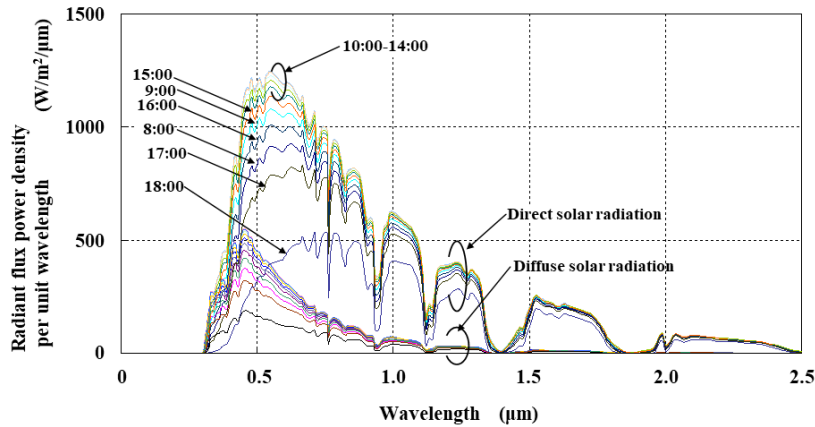
### 10.2.7. Direct Solar Radiation and Diffuse Solar Radiation

Fig. 10.12 shows the daytime variations in direct solar radiation and diffuse solar radiation on the horizontal ground plane simulated using the “SPECTRAL2” solar spectrum model by Bird and Riordan [79]. Detailed simulated conditions are as follows: longitude =  $137^{\circ}3'E$  and latitude =  $35^{\circ}10'N$ , August 1<sup>st</sup>, AM1.5, total column ozone = 0.34 cm, total precipitable water vapor = 1.34 cm, and aerosol optical depth at the wavelength of 500 nm = 0.27. It can be observed in the figure that the shape of the spectrum of the diffuse solar radiation does not vary but its intensity varies with time. In contrast to this, the spectra of the direct solar radiation shows a significant red shift with time in the afternoon. The effects of this spectrum shift must be seriously considered in the case of SPLs because they mainly work with direct solar radiation. If an aplanatic lens is used for solar concentration, the spectrum shift in the afternoon may affect the SPL oscillation in connection with the chromatic aberration of the lens. The spectrum shift may also affect the SPL oscillation in connection with the absorption and excitation spectra of the LM. The total radiant flux power density between wavelengths of 300 nm and  $4\ \mu\text{m}$  can be calculated as follows:

- Global solar radiation:  $1008\ \text{W/m}^2$  (100 %);
- Direct solar radiation:  $787\ \text{W/m}^2$  (78 %);
- Diffuse solar radiation:  $221\ \text{W/m}^2$  (22 %).

In a typical case in which a Cr,Nd:YAG transparent ceramic LM is employed, the total radiant flux density is considerably reduced because the wavelength range of the absorption spectrum is reduced to being between 300 nm and 900 nm, as shown below:

- Global solar radiation:  $696\ \text{W/m}^2$  (100 %);
- Direct solar radiation:  $508\ \text{W/m}^2$  (73 %);
- Diffuse solar radiation:  $188\ \text{W/m}^2$  (27 %).



**Fig. 10.12.** Daytime variations of solar spectrum for direct solar and diffuse solar radiations on the horizontal ground plane simulated using the “SPECTRAL2” solar spectrum model by Bird and Riordan [79] for longitude =  $137^{\circ}3'E$  and latitude =  $35^{\circ}10'N$ , August 1<sup>st</sup>, AM1.5, equivalent ozone depth = 0.34 cm, total precipitable water vapor = 1.34 cm, and aerosol optical depth =  $0.27@500\text{ nm}$ .

On an inclined plane or on a plane with its surface normal tracking the Sun, the total radiant flux density can be improved. Fig. 10.13 shows daytime variations of global solar radiation power density (1) on a horizontal plane, (2) on a plane inclined south at  $37^{\circ}$  to the horizontal plane, (3) on a plane with its surface normal tracking the Sun, and (4) direct solar radiation on a plane with its surface normal tracking the Sun, calculated using the “SPECTRAL2” solar spectrum model by Bird and Riordan [79] for longitude =  $137^{\circ}3'E$  and latitude =  $35^{\circ}10'N$ , under typical clear skies, on a Spring/Autumn day, with diffuse fraction = 25 %, and transmittance of the atmospheric layer = 75 %. Fig. 10.13 shows that sun-tracking can gain larger solar radiation both in the morning and in the afternoon. The following integrated solar radiation power densities throughout the day also show the advantages of sun-tracking:

- Global, on the horizontal plane:  $6462\text{ Wh/m}^2$ ;
- Global, on the plane inclined south at  $37^{\circ}$  to the horizontal plane:  $6530\text{ Wh/m}^2$ ;
- Global, tracking the Sun:  $8572\text{ Wh/m}^2$ ;
- Direct, tracking the Sun:  $6940\text{ Wh/m}^2$ .

In Subsection 10.2.2, a typical threshold power for oscillation of Nd:YAG laser was calculated to be approximately  $5500\text{ kW/m}^2$ . As described in Subsection 10.2.4, in actual practice, solar concentration ratios are between 12.5 % and 45 % of the theoretical upper limit of 46200. Therefore, the radiant flux power density is  $5775\text{--}20790\text{ kW/m}^2$  when the direct solar radiation was  $1\text{ kW/m}^2$ . Therefore, the direct solar radiation utilized by Cr, Nd:YAG at noon ( $508\text{ W/m}^2$ ) can make the practical concentrated radiant flux power density =  $2994\text{--}10561\text{ kW/m}^2$ . This shows that it is important to use lenses or mirrors of larger  $D/f$  and higher transmittance or reflectivity for stable oscillation in the daytime – almost from sunrise to sunset – tracking the Sun.

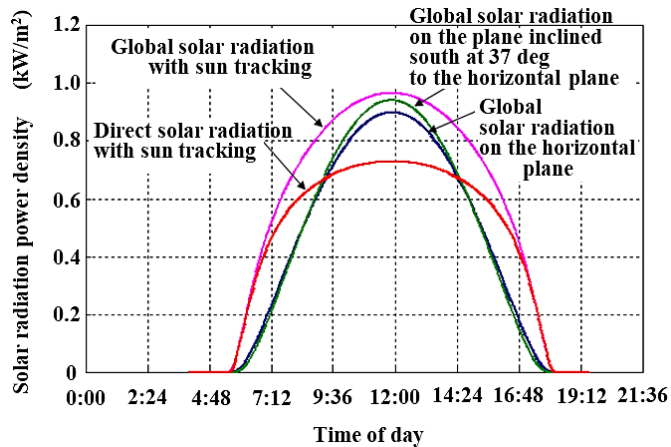


**Fig. 10.13.** Daytime variations of global solar radiation power density (1) on a horizontal plane (a black line), (2) on a plane inclined south at  $37^\circ$  to the horizontal plane (a green line), (3) on a plane with its surface normal tracking the Sun (a pink line) and (4) direct solar radiation on a plane with its surface normal tracking the Sun (a red line). Simulations were performed using the solar spectrum model “SPECTRAL2” by Bird and Riordan [79] for longitude =  $137^\circ 3'E$  and latitude =  $35^\circ 10'N$ , under typical clear skies, on a Spring/Autumn day, with the diffuse fraction = 25 %, and the transmittance of the atmospheric layer = 75 %.

We also measured the direct solar radiation on Wednesday, August 9<sup>th</sup>, 2017 on the ground at  $136^\circ 58'E$  longitude and  $35^\circ 10'N$  latitude (Nagoya, Japan) using a pyrheliometer for the direct solar radiation of  $\varnothing 18$  mm caliber mounted on an equatorial mounting that tracked the Sun. The power of the direct solar radiation in the view angle of  $5^\circ$  and in the wavelength range of 190 to 25000 nm captured with an aperture and a pinhole was measured with a THOLABS S302C thermal power meter sensor attached to the pyrheliometer, as shown in Fig. 10.14. The THOLABS S302C power meter sensor had been calibrated with an EKO INSTRUMENTS MS-53 (ISO 9060 First Class Pyrheliometer), which provided the value of the direct solar radiation in terms of  $W/m^2$ . The measured value was  $905 W/m^2$  for similar conditions in which  $787 W/m^2$  was obtained via SPECTRAL2.



**Fig. 10.14.** A THOLABS S302C thermal power meter sensor with a pinhole calibrated and attached to a pyrheliometer.

We also monitored the daytime variations of the solar spectrum change using an Ocean Optics MAYA2000 solid-state optical spectrum analyzer. Fig. 10.15 shows variation in the measured solar spectrum as a function of the clock time. The shapes of the spectra qualitatively show a gradual red shift of the peak of the solar spectrum as the afternoon grew late, similar to the results obtained from the “SPECTRAL2” solar spectrum model shown in Fig. 10.12. Therefore, chromatic aberration must also be reduced in an aplanatic lens for solar concentration because of the wide-band range of the solar spectrum and its red shift with elapse of the time of the day. However, achromatic aplanatic lenses are not cost-effective. Therefore, parabolic mirrors are preferable as solar concentrators for SPLs. However, large-scale parabolic mirrors are also not cost-effective. Therefore, the preferable choice for the solar concentrator will be a small parabolic mirror.

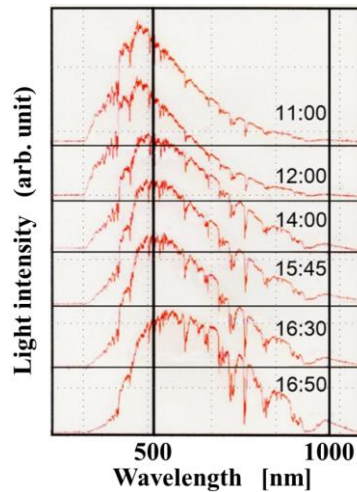


Fig. 10.15. Variation in the measured solar spectrum as a function of the clock time.

### 10.3. Compact Solar-Pumped Fiber Laser (SPFL) System

#### 10.3.1. Choice of Laser Mediums (LMs)

##### 10.3.1.1. Shape of LMs

As described in Subsection 10.2.3, either disk-like and fiber-like shapes are advantageous for LMs from the point of efficient excitation and efficient thermal dissipation. As described in Subsection 10.2.1, solar-pumped lasers utilizing emissions from Nd ions are preferable practical systems in the case of a single wavelength emission type because their emission wavelength  $\lambda_L$  (approximately  $1.06 \mu\text{m}$ ) is near the optimal wavelength region situated between 1100 and 1300 nm, as shown in Fig. 10.1(b). So far as the LMs utilizing emissions from Nd ions is concerned, the long optical path of a fiber-type LM enables absorption of almost all the pumping light propagating along its axial direction. In contrast, the short interaction length of a disk-type LM is insufficient for the same amount

of pumping sunlight to be absorbed. Therefore, a fiber-type LM was chosen to develop a solar-pumped fiber laser (SPFL).

### 10.3.1.2. Glass LMs

To realize a fiber-type LM as well as a disk-type LM, it was suggested in Subsection 10.2.3 that glass LMs are promising for SPLs because of their high moldability into thin disks/thin fibers, high solubility of rare-earth elements such as Nd, and suitability for mass production.

Thus,  $\text{TeO}_2\text{-K}_2\text{O}$  (tellurite) glass,  $\text{SiO}_2\text{-B}_2\text{O}_3\text{-Na}_2\text{O-Al}_2\text{O}_3\text{-CaO-ZrO}_2$  (SBNACZ, borosilicate) glass, and  $\text{ZrF}_4\text{-BaF}_2\text{-LaF}_3\text{-AlF}_3\text{-NaF}$  (ZBLAN, fluoride) glass were examined as host glasses [80]. The content of Nd was changed in the range of 0-5.0 mol %.  $\text{TeO}_2\text{-K}_2\text{O}$  (tellurite) glass has the advantage of having the largest integrated absorption cross-section of  $\text{Nd}^{3+}$  from 400 to 950 nm among the approximately 250 glass hosts. For example, it is about 1.5 times higher than those in borosilicate glass and fluoride glass [81, 82]. The effective phonon energy in tellurite glass is usually less than  $800\text{ cm}^{-1}$ , which is lower than that of the other oxides such as silicate ( $1000\text{ cm}^{-1}$ ) and phosphate ( $1200\text{ cm}^{-1}$ ) [83]. This enables efficient fluorescence from  $\text{Nd}^{3+}$  ions doped in the tellurite glass. SBNACZ borosilicate glass has the advantage of having excellent rare-earth solubility and chemical and thermal stability against crystallization because of its high glass transformation temperature. Crystallization behavior was not noticed for rare-earth doping less than 10 wt. %. Therefore, it was initially suggested as a host medium to immobilize high level nuclear waste [84]. SBNACZ borosilicate glass can hold up to 30 wt. %  $\text{Nd}_2\text{O}_3$  without evidence of Nd clustering and has been proposed as an LM [81, 82]. ZBLAN fluoride glass, found in 1975 [85], has advantages in terms of its wide transparent window between 0.22 and about  $8\text{ }\mu\text{m}$ , low minimum loss as low as  $1\text{ dB/km}$  [86], low effective phonon energy of less than  $600\text{ cm}^{-1}$  [87], and high allowable doping levels (up to 10 mol %) of rare-earth ions [34].

The internal quantum efficiencies under sunlight tracking the Sun using an altazimuth and Ti:sapphire laser excitation (at 807 nm for tellurite and borosilicate glasses and at 794 nm for fluoride glass) were measured directly using an integrating sphere method (cf. Fig. 10.22 (a)). The radiative quantum efficiency obtained by Judd-Ofelt analysis was almost 100 % for the tellurite and ZBLAN fluoride glasses and 50 % for the SBNACS borosilicate glasses. The quantum efficiency under laser excitation was respectively found to be 86 %, 34 %, and 88 % for the tellurite, SBNACS borosilicate, and ZBLAN fluoride glasses at a low  $\text{Nd}^{3+}$  content. Parasitic absorption in the SBNACZ borosilicate glass might have caused the low quantum efficiency. The quantum efficiency under sunlight excitation was up to 33 %, 21 %, and 70 % for the tellurite, SBNACS borosilicate, and ZBLAN fluoride glasses, respectively. Therefore, ZBLAN fluoride glass was chosen for the glass LM. The stimulated emission cross-section  $\sigma(\lambda_L)$  in the transition  ${}^4\text{F}_{3/2}$  to  ${}^4\text{I}_{11/2}$  corresponding to the 1064 nm emission for 0.5 mol. %  $\text{Nd}^{3+}$  doped in ZBLAN glass was calculated to be  $2.95 \times 10^{-20}\text{ cm}^2$ . With a fluorescence lifetime = 496  $\mu\text{sec}$  for glass,  $\sigma(\lambda_L) \cdot \tau$  was obtained to be  $1.46 \times 10^{-27}\text{ m}^2\text{s}$ , which is higher than  $0.75 \times 10^{-27}\text{ m}^2\text{sec}$  for Nd-doped silica glass codoped with Al [88].



The offset angle of this OAP was  $90^\circ$ . The focal point F is located on the horizontal line, which penetrates the center point O of the OAP. The distance between F and O was also designed to be 50.8 mm. Among the commercially available products of  $\varnothing 50.8$  mm caliber OAP, this was of the shortest FO length. Based on the geometrical consideration in Fig. 10.16 (a), the length of the inverted image of the black arrow  $d$  can be given as

$$d = \left( \frac{D}{A_u} \right) \cdot \frac{2D}{1 - \frac{12}{5} \cdot \frac{D}{A_u}} \quad (10.24)$$

Supposing the ratio of the length of the image of the white arrow-shaped object  $r_s$  to  $d$  is the same as the ratio  $R_s$  to  $D$ ,  $r_s$  can be given as

$$r_s = d \cdot \frac{R_s}{D} = \left( \frac{R_s}{A_u} \right) \cdot \frac{2D}{1 - \frac{12}{5} \cdot \frac{D}{A_u}} \cong \left( \frac{R_s}{A_u} \right) \cdot 2D \quad (10.25)$$

Here,  $D/A_u \ll 1$  is used for the approximation. The lateral location of the image is defined by the distance from F,  $x$ , which can be expressed as

$$x = \frac{12}{5} \cdot \left( \frac{D}{A_u} \right) \cdot 2D \quad (10.26)$$

Because  $D/A_u \ll 1$ , the image is located at  $x \approx 0$ , that is, on the focal point F. Similarly, based on geometrical consideration in Fig. 10.16 (b), the length of the inverted image of the black arrow  $d$  can be expressed similar to Eq. (10.24). As for the lateral location of the image,  $x$  is obtained as follows:

$$x = \frac{4}{3} \cdot \left( \frac{D}{A_u} \right) \cdot 2D \quad (10.27)$$

Because  $D/A_u \ll 1$ , both the images in Figs. 10.16 (a) and (b) are located at  $x \approx 0$ , that is, on the focal point F, as indicated in Eqs. (10.26) and (10.27). Figs. 10.16 (c) and (d) show the side view and front view for cases in which the arrow-shaped objects are pointing perpendicular to the plane of paper, respectively. Traces of two typical light rays emitted from the head of the black arrow drawn on the white arrow-shaped object are indicated with blue and red lines. It is shown that the two lines, blue and red, do not intersect with each other at a point three-dimensionally. More specifically, the red ray penetrates the focal point F but the blue ray does not. This is because the present OAP is not precisely an imaging system. However, the blue ray passes near the focal point. At the point of the nearest approach, the distance from F is  $(D/A_u) \cdot 2D$ . As for the light ray emitted from the head of the white arrow-shaped object corresponding to the blue line, the distance between the point of the nearest approach and F can be calculated as  $(R_s/A_u) \cdot 2D$ . This is the same as Eq. (10.25). Therefore, all incident sunlight at the entrance of the OAP crosses inside

the circle of radius  $r_s$  at the focal point F. Therefore,  $2r_s$  is not a diameter of the image of the Sun. It should be called the diameter of the pseudo image of the Sun. The solar concentration ratio can be expressed as follows:

$$\frac{\pi D^2}{\pi r_s^2} = \frac{D^2}{\left(\frac{R_s}{A_u}\right)^2 \cdot 4D^2} = \left(\frac{A_u}{R_s}\right)^2 \cdot \frac{1}{4} \quad (10.28)$$

Using 50.8 mm for  $2D$ ,  $6.96 \times 10^8$  m for  $R_s$ , and  $1.496 \times 10^{11}$  m for  $A_u$  into Eqs. (10.25) and (10.28), the diameter of the pseudo image of the Sun and corresponding solar concentration ratio can be obtained as follows:

$$2r_s = 0.473 \text{ mm}, \quad (10.29)$$

$$\frac{\pi D^2}{\pi r_s^2} = 11550 \quad (10.30)$$

### 10.3.3. SPL Resonator Based on a Double Cladding Optical Fiber

Using the OAP in Fig. 10.16, the diameter of the image of the Sun near the focal point is 0.473 mm as shown in Eq. (10.29). A double-clad fiber (DCF) structure composed of a core ( $\varnothing 5 \mu\text{m}$ ), an inner cladding ( $\varnothing 125 \mu\text{m}$ ), and an outer cladding ( $\varnothing 200 \mu\text{m}$ ) was employed. Both end facets were coated with thin film mirrors having reflectivity of 98 % at 1050 nm [30-32]. A substantial part of the focused sunlight that hits out of the core can enter the inner cladding and propagates in it, after which it eventually enters the core to be absorbed by ions in the core as schematically shown in Fig. 10.17(a). This 10 m long Nd 0.5 at% doped ZBLAN DCF was spooled on a kidney-shaped spool to increase the chance of sunlight propagating in the inner cladding to enter the core. As a consequence, the mode-matching efficiency is as high as 80 %. The absorption spectrum, in comparison with the broadband solar spectrum, gives the spectrum matching efficiency of absorption of 13 %. Fig. 10.17 (b) shows a schematic diagram of this SPFL system. Fig. 10.18 shows photographs of this SPFL system mounted on an altazimuth-type solar-tracking system (Vixen SKYPOD).

In this system, the factor in the first parenthesis in Eq. (10.8),  $h \cdot \nu_e / (\sigma(\lambda_L) \cdot \tau)$ , is  $1.69 \times 10^5 \text{ kW/m}^2$ . Supposing 0.8 for  $\delta$ , and using 0.98 for  $R_1$  and  $R_2$ , the factor in the second parenthesis in Eq. (10.31),  $(\delta - \ln(R_1 \cdot R_2))/2$ , is 0.42. Supposing 0.62 ( $= 650 \text{ nm} / 1050 \text{ nm}$ ) for  $\eta_{QD}$ , 1 for  $\eta_{QE}$ , 0.13 for  $\eta_{\text{abs}}$ , 0.8 for  $\eta_m$ ,  $4 \times 10^6$  ( $= 10 \text{ m} / 2.5 \mu\text{m}$ ) for  $A$ , and  $2 \times 10^{-4}$  ( $= 2 \text{ mm} / 10 \text{ m}$ ) for  $\alpha$  (assuming 2 mm of cladding from the end facet functions effectively), the threshold power density is calculated to be  $686 \text{ kW/m}^2$ . Supposing the incident direct solar radiation is  $508 \text{ W/m}^2$  as described in Subsection 10.2.7, and geometrical and reflectivity loss of the solar concentrator is 30 %, the required concentration ratio is 1930 ( $686 \text{ kW/m}^2 / (0.508 \text{ kW/m}^2 \times 0.7)$ ). Therefore, it was conjectured that the system shown in Figs. 10.17 and 10.18 has a good chance to realize oscillation.

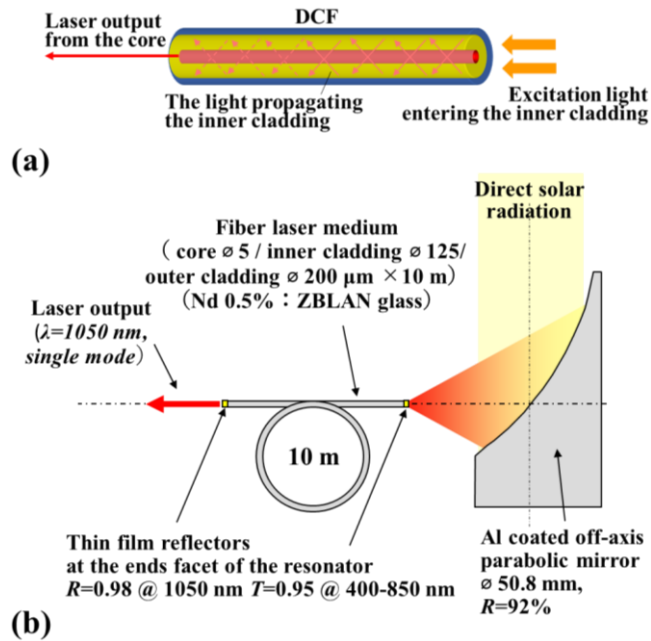


**Fig. 10.17.** Schematic diagrams of (a) double clad optical fiber (DCF), and (b) a prototype SPFL system composed of OAP and Nd 0.5 at% doped ZBLAN DCF laser medium.

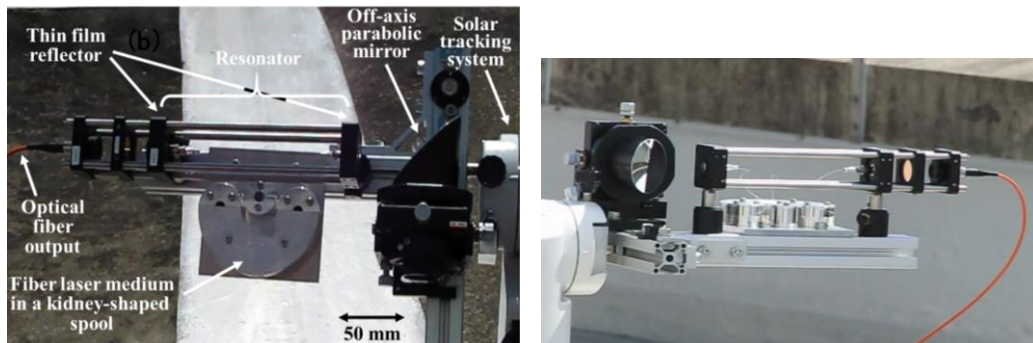


**Fig. 10.18.** Photographs of the prototype SPFL system comprising an OAP, a kidney-shaped spool for a 10 m long Nd 0.5 at% doped ZBLAN DCF, and an optical fiber for the SPFL output. The system is mounted on an altazimuth type solar-tracking system.

### 10.3.4. Outdoor Oscillation Performance of the Compact SPFL

Lasing experiments using sunlight were performed at longitude 137°3'E and latitude 35°10'N under clear skies with occasional cumuli. Fig. 10.19 (a) shows the direct sunlight spectrum and the measured spectrum after passing through the Nd 0.5 at% -doped ZBLAN fluoride glass fiber together with the lasing spectrum. The direct sunlight spectrum was calculated according to the model by Bird and Riordan [79] under the following conditions: elevation angle = 37°, aerosol optical depth at 500 nm wavelength = 0.27, total

column ozone = 0.34 cm, surface albedo = 0.20, total precipitable water vapor = 1.42 cm, longitude = 137° 3' E, and latitude = 35° 10' N. Absorption bands observed were indicated with the identified related excited electronic levels of Nd<sup>3+</sup> ion. Sunlight was completely absorbed around the bands at wavelengths of 520 nm, 575 nm, 740 nm, 795 nm, and 867 nm. However, strong intensity transmissions, such as blue light with wavelengths between 410 nm and 510 nm and red light with wavelengths between 590 nm and 725 nm, still remain. The detailed lasing spectra around 1053.7 nm obtained at different times are shown in Fig. 10.19(b). Many peaks were observed between 1052 nm and 1054 nm. Typically, the full width of the half maximum of the peak at 1053.7 nm is approximately 0.01 nm. The spectra showed a complex and congested nature and fluctuated quickly. This was caused partly because of inhomogeneous broadening from Nd ions in glass and longitudinal-mode hopping.

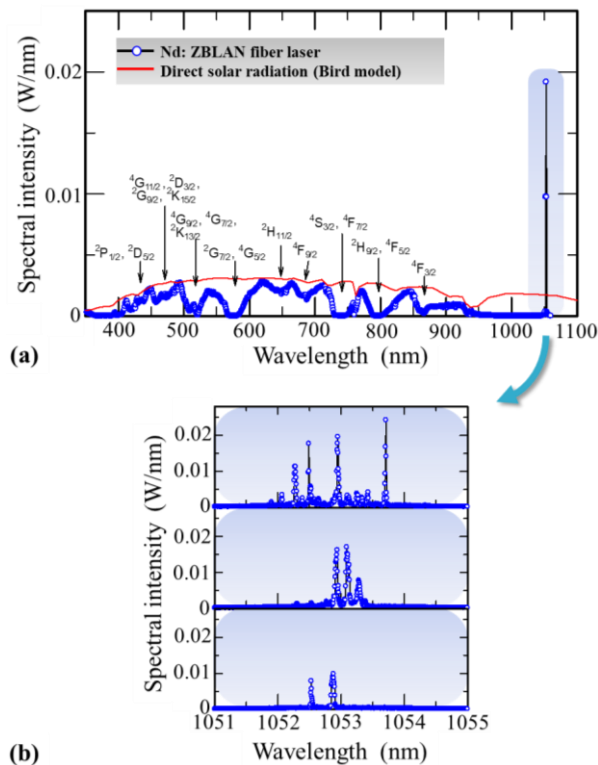


**Fig. 10.19.** (a) The direct sunlight spectrum (in red) and the measured spectrum after passing through the Nd 0.5 at% -doped ZBLAN fluoride glass fiber together with the lasing spectrum (in blue open circles). The locations of absorption bands are indicated with the identified related excited electronic levels of Nd<sup>3+</sup> ion. (b) Detailed lasing spectra around 1053.7 nm obtained at different times.

Fig. 10.20 shows the plots of the SPFL output power as a function of the input sunlight power captured in the inner cladding of the fiber. The input sunlight power was controlled by changing the flare angle of the bow-tie aperture placed at the sleeve for the parabolic

mirror (cf. Fig. 10.26). A clear lasing threshold at 49.1 mW is confirmed by natural sunlight excitation. The slope efficiency and the total efficiency were 3.3 % and 0.88 %, respectively. The maximum laser output power was 0.57 mW. Because the reflectivity of both ends of the fiber are the same, adding the output powers from both ends, the slope efficiency and the total efficiency are doubled to be 6.6 % and 1.76 %, respectively [34]. This is “the first solar-pumped fibre laser” as picked up by *Nature Materials* [89].

The threshold power was derived to be 49.1 mW. Dividing the cross-sectional area within  $\varnothing 125 \mu\text{m}$  of the inner cladding and the core of the ZBLAN optical fiber, the threshold power density  $I_{\text{eth}}$  at the end facet of the fiber to start laser oscillation is approximately  $4 \text{ MW}/\text{m}^2$ . Passing through the preposing optical system including a UV filter with a transmittance of 95 % and OAP with a reflectance of 92 %, the total transmittance of the preposing optical system was 71.5 %. Taking the solar concentration ratio (11550) of this OAP into consideration, the power density before the concentration is  $484 \text{ W}/\text{m}^2$ . Similarly, the maximum sunlight power density in this measurement was obtained as  $651 \text{ W}/\text{m}^2$ . In the example of a numerical estimate based on the Eq. (10.8) in Subsection 10.2.2,  $I_{\text{eth}}$  was estimated to be about  $686 \text{ kW}/\text{m}^2$ , which is much less than the experimentally obtained value of  $4 \text{ MW}/\text{m}^2$ . It is conjectured that a larger value of  $\delta$  and smaller value of  $\eta_{\text{QD}}$ ,  $\eta_{\text{QE}}$ ,  $\eta_{\text{abs}}$ ,  $\eta_{\text{m}}$  and  $\alpha$  in practice may have caused this result.

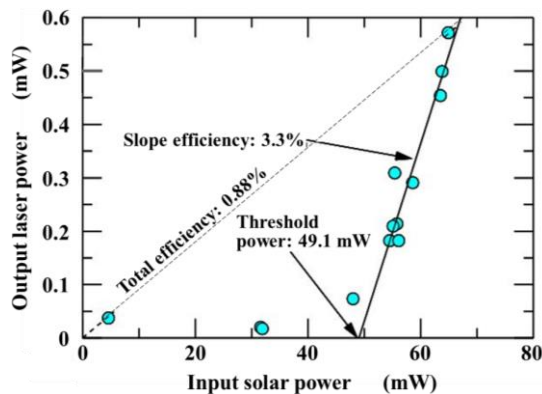
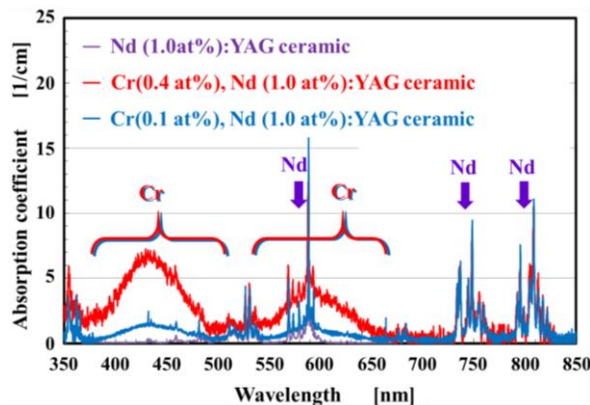


Fig. 10.20. Output laser power of SPFL as a function of input solar power.

#### 10.4. Improvement of Spectral Matching Efficiency by Cr Codoping

The spectral absorption range of the LM should cover a wide spectral range of sunlight – from UV to IR. This is referred to as “spectral matching”. It has been considered that an SPL using a single rare-earth element such as Nd cannot be efficiently driven because of the extremely narrow absorption bands of rare-earth elements [23]. A promising means for the improvement of spectrum matching is to introduce a sensitizer of another element that extends the absorption range considerably [90]. Particularly, it has been found that the transition metal  $\text{Cr}^{3+}$  is a promising sensitizer, which has broadband absorption characteristics and transfers the absorbed energy to  $\text{Nd}^{3+}$  [20, 42, 58, 63, 91-97]. In our ZBLAN fiber, the mode-matching efficiency  $\eta_{\text{m}}$  is as high as 80 % while the spectral

matching efficiency  $\eta_{\text{abs}}$  is 13 %. Therefore, it is important to increase the spectral matching efficiency by Cr codoping in addition to Nd. Although  $\text{Cr}^{3+}$  codoping is a possible tactic to improve the performance of SPFL, it was eventually found difficult to codope Cr into Nd-doped ZBLAN fibers. Therefore, instead of taking advantage of the large aspect ratio  $A$  of fiber LMs shown in Fig. 10.6, we used Cr-codoped Nd:YAG transparent ceramic micro rods to make use of the advantages described in Subsection 10.2.6 and Fig. 10.11. Fig. 10.21 shows the measured spectral absorption coefficients of transparent ceramic mediums of (1) Nd (1.0 at%):YAG, (2) Cr (0.1 at%), Nd (1.0 at%):YAG, and (3) Cr (0.4 at%), Nd (1.0 at%): YAG. In contrast with the narrow adsorption peaks of (1) Nd (1.0 at%):YAG, (2) Cr (0.1 at%), Nd (1.0 at%):YAG and (3) Cr (0.4 at%), Nd (1.0 at%):YAG showed broad absorption peaks. It was also shown that the increase in Cr content from 0.1 at% to 0.4 at% caused an approximate 4 times increase in the broad absorption peaks. It is expected that spectral matching efficiency improves from 13 % to 35 % by the codoping of Cr ions. Then, introducing sunlight into an integrating sphere, spectral absorption, and emission properties of Nd:YAG and Cr-codoped Nd:YAG were examined. Fig. 10.22 (a) schematically shows a system to measure the spectral absorption and emission from the sample in an integrating sphere in the wavelength range of 300 nm to 1600 nm under natural sunlight irradiation (LUCIR FQEM-L1). Fig. 10.22 (b) shows the observed spectra with and without a sample. Subtracting the spectrum without a sample from the spectrum with a sample, a differential spectrum could be obtained that showed absorption of the solar spectrum and the spontaneous emission from the sample. Fig. 10.22 (c) shows a differential spectrum measured for the Nd (1 at%):YAG ceramic sample, which shows absorption of the solar spectrum and emission (1064 nm) from  $\text{Nd}^{3+}$  ions. Fig. 10.22 (d) shows a similar differential spectrum for Cr (0.5 at%)-codoped Nd (1 at%):YAG ceramics sample. In comparison with the spectrum in Fig. 10.22 (c), the absorption of the solar spectrum was enhanced, and the emission (1064 nm) increased 1.5 times in Fig. 10.22 (d). This indicates the photon energies absorbed by  $\text{Cr}^{3+}$  ions were transferred to  $\text{Nd}^{3+}$  ions and contributed the spontaneous photoemission. Thus, Cr doping to Nd:YAG transparent ceramic rod was experimentally reconfirmed to be a promising tactic to improve SPLs.



**Fig. 10.21.** Measured spectral absorption coefficients of transparent ceramic mediums of (1) Nd (1.0 at%): YAG; (2) Cr (0.1 at%), Nd (1.0 at%): YAG; and (3) Cr (0.4 at%), Nd (1.0 at%): YAG.

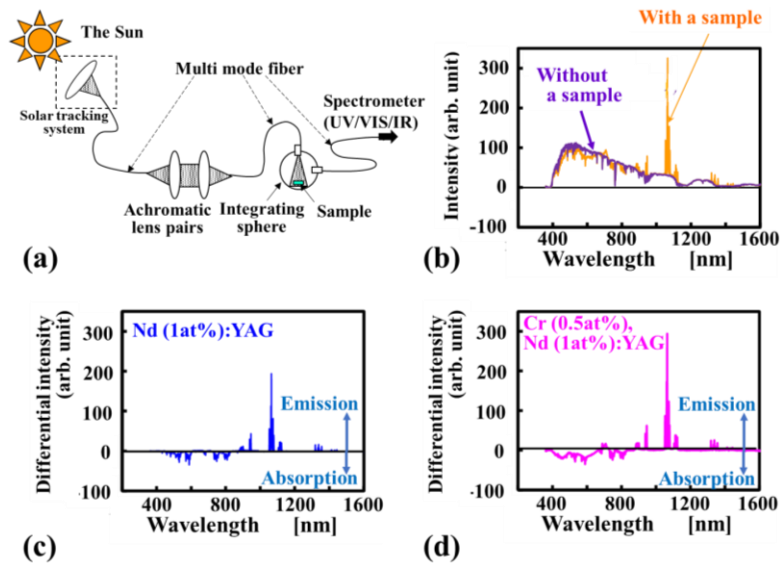


**Fig. 10.22.** Measurement of differential spectra showing absorption of sunlight and spontaneous emission from Nd:YAG ceramic samples and Cr-codoped Nd:YAG ceramic samples by guiding the natural sunlight into an integrating sphere using a solar-tracking system and optical fibers.

### 10.5. Compact Solar-Pumped Micro-Rod Laser ( $\mu$ SPL) System

We replaced the Nd-doped ZBLAN glass fiber with a  $1 \times 1 \times 5$  mm quadrangular-prism-shaped, Cr 0.1 at% codoped, Nd 1 at%:YAG transparent ceramic micro laser rod supplied by World Lab. Co. Ltd, Japan as shown in Fig. 10.23.

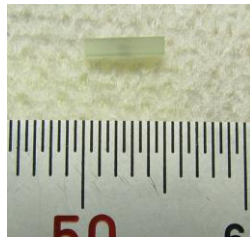


**Fig. 10.23.**  $1 \times 1 \times 5$  mm, Cr 0.1 at% codoped, Nd 1 at%:YAG transparent ceramic micro laser rod.

The solar concentrator was changed to a  $\varnothing 76.2$  mm caliber OAP (Edmund Optics) keeping the distance between the focus F and the center of OAP, O, unchanged from that of the  $\varnothing 50.8$  mm caliber OAP used in the SPFL described in Section 10.3, that is, 50.8 mm. Among the commercially available products of  $\varnothing 76.2$  mm caliber OAP, this is of the shortest OF length. Expressing the caliber diameter 76.2 mm as  $2D$  in this section, the distance between F and O is  $4D/3$  as shown in the schematic drawing Fig. 10.24, which is

drawn in the same manner as Fig. 10.16. Based on the geometrical consideration in Fig. 10.24(a), the length of the inverted image of the white arrow-shaped object  $r_s$  is obtained using a similar process as the derivation of Eq. (10.25):

$$r_s \cong \left( \frac{R_s}{A_u} \right) \cdot \frac{4}{3} D \quad (10.31)$$

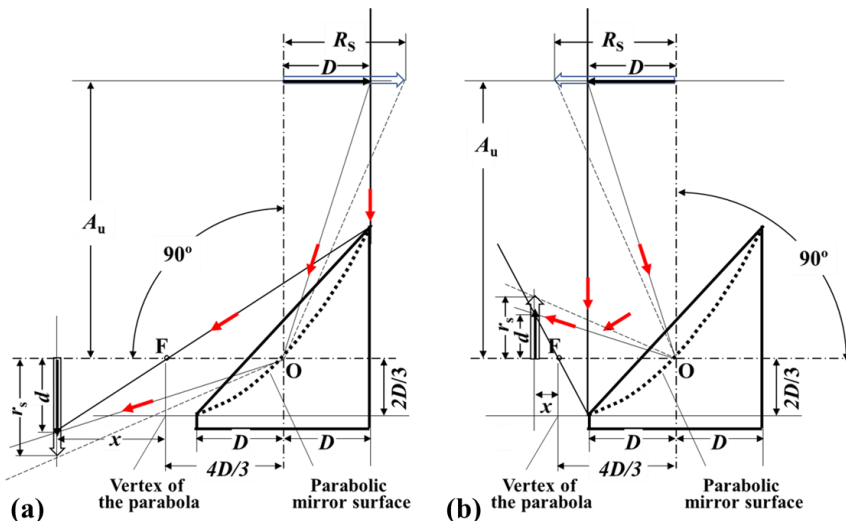
The same result is also obtained from Fig. 10.24(b). Then, it can be shown that all the incident sunlight at the entrance of the OAP crosses inside the circle of radius  $r_s$  at the focal point F in the same manner as shown in Subsection 10.3.2. The solar concentration ratio can be expressed as follows:

$$\frac{\pi D^2}{\pi r_s^2} = \frac{D^2}{\left( \frac{R_s}{A_u} \right)^2 \cdot \left( \frac{4}{3} \right)^2 \cdot D^2} = \left( \frac{A_u}{R_s} \right)^2 \cdot \frac{9}{16} \quad (10.32)$$

Using values 36.1 mm for  $D$ ,  $6.96 \times 10^8$  m for  $R_s$ , and  $1.496 \times 10^{11}$  m for  $A_u$  into Eqs. (10.31) and (10.32):

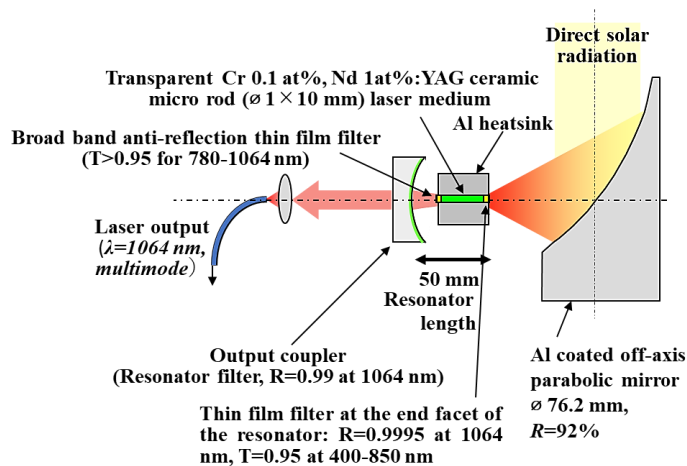
$$2r_s = 0.448 \text{ mm}, \quad (10.33)$$

$$\frac{\pi D^2}{\pi r_s^2} = 25990 \quad (10.34)$$



**Fig. 10.24.** Schematic drawings of an OAP of a caliber diameter  $2D$  of 76.2 mm with typical traces of light rays emitted from the head of a white arrow-shaped object of a length  $R_s$  and the head of a black arrow drawn on the white arrow-shaped object of a length  $D$ . (a) A case in which the arrow-shaped object is pointing right in a side view of the system, (b) A case in which the arrow-shaped object is pointing left in a side view of the system.

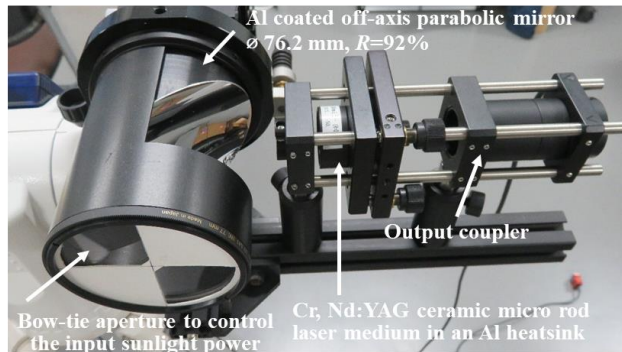
These results are more favorable than the results for the  $\varnothing 50.8$  mm caliber OAP shown in Eqs. (10.29) and (10.30). Sunlight can be focused within the end facet of the  $\varnothing 1 \times 10$  mm rod. Fig. 10.25 schematically shows this  $\mu$ SPL system. Output coupler (OC) of different curvature radii were tested. In a typical case of Nd:YAG laser where  $\lambda_L$  was 1064 nm,  $\lambda_e$  was 808 nm,  $\sigma(\lambda_L)$  was  $2.8 \times 10^{-19}$  cm<sup>2</sup>,  $\tau$  was 230  $\mu$ sec [98],  $\delta$  was 0.02,  $R_1$  was 0.99,  $R_2$  was 0.9995,  $\eta_{QD}$  was 0.61 (= 650 nm / 1064 nm),  $\eta_{QE}$  was 1,  $\eta_{abs}$  was 0.35,  $\eta_m$  was 0.29,  $A$  was 10 (5 mm / 0.5 mm) and  $\alpha$  was 0.03,  $I_{eth}$  was calculated to be 5.9 MW/m<sup>2</sup>. Therefore, solar concentration ratio of more than 16244 is required for the direct solar radiation of 508 W/m<sup>2</sup> to start oscillation of this laser rod, taking the transmittance of the preposing optical system to 71.5 % including a UV filter with a transmittance of 95 %, and OAP with a reflectance of 92 %. Fig. 10.26 shows a photograph of the nucleus of a  $\mu$ SPL. Bow-tie apertures of different flare angles were used to control the incident sunlight power to measure the input solar power dependence of the output laser power. Fig. 10.27 shows the  $\mu$ SPL system mounted on an altazimuth-type solar-tracking system (Vixen SKYPOD) in an outdoor oscillation experiment tracking the Sun. The  $\mu$ SPL is compact enough to use an altazimuth fabricated to mount an astronomical telescope for observation of celestial objects (Vixen SKYPOD) as a solar-tracking system.



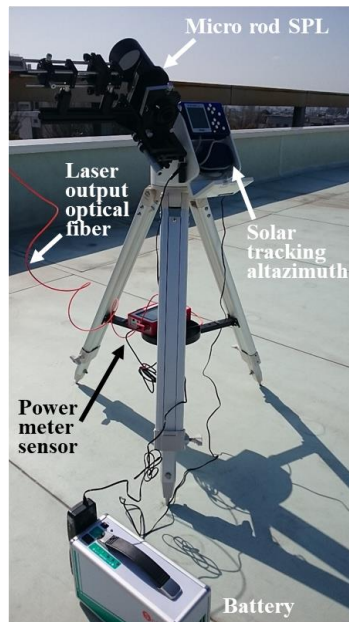
**Fig. 10.25.** Schematic diagrams of a prototype  $\mu$ SPL system comprised of an OAP and a Cr 0.1 at%, Nd 1 at% doped transparent YAG ceramic rod laser medium in an Al heat sink, an OC, and an optical fiber for laser output.

Fig. 10.28 (a) shows the measured output laser power as a function of the input solar power into the rod shown in the abscissa at the bottom. An OC of a curvature radius = 100 mm was used. The input solar power into the OAP is also indicated in the abscissa at the top. The maximum input solar power into the OAP was 4.28 W, which corresponds to a direct solar radiation of 939 W/m<sup>2</sup>. Passing through the preposing optical system, including a UV filter with a transmittance of 95 % and OAP with a reflectance of 92 %, the maximum input solar power into the rod was 3.06 W. The total transmittance of the preposing optical system was 71.5 %. The threshold power at the end facet of the rod was 1.8 W. Dividing it by the area of the focused size,  $\pi \cdot r_s^2$  of  $1.58 \times 10^{-7}$  m<sup>2</sup>, the threshold

power density of  $11.4 \text{ MW/m}^2$  could be obtained. The slope efficiency against the input solar power at the rod and the total efficiency against the input solar power at the rod were 2.1 % and 0.9 %, respectively. The external slope efficiency and the external total solar conversion efficiency against the input solar power into the OAP were 1.5 % and 0.7 %, respectively. Fig. 10.28(b) shows optical transmittance spectra of sunlight before and after passing through the laser rod. The difference between the two spectra corresponds to the absorbed light by the rod. Fig. 10.28 (c) shows the laser emission spectrum peaking at 1064 nm.



**Fig. 10.26.** Nucleus of the  $\mu$ SPL system composed of an OAP and a resonator comprising a Cr-codoped, Nd:YAG transparent ceramic micro laser rod and an optical coupler. Bow-tie apertures of different flare angles are used for controlling the incident sunlight power to measure the input solar power dependence of the output laser power.



**Fig. 10.27.** Outdoor oscillation experiment of a  $\mu$ SPL on an altazimuth tracking the Sun.

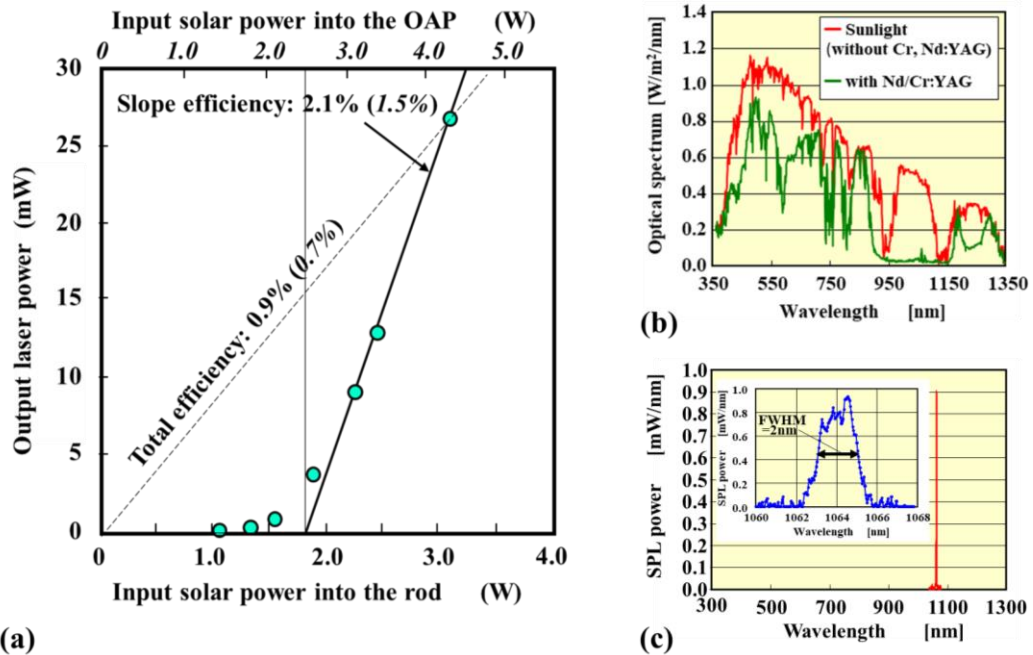


**Fig. 10.28.** (a) Output laser power of a  $1 \times 1 \times 5$  mm Cr (0.1 at%), Nd (1 %):YAG transparent ceramic rod type  $\mu$ SPL as a function of the input solar power; (b) Optical transmittance spectra of sunlight before and after passing through the laser rod; (c) Spectrum of the output laser. The inset figure shows a detailed peak profile between 1060 nm and 1068 nm.

Fig. 10.29 shows the measured output laser power as a function of the input solar power into the  $\varnothing 1 \times 10$  mm, Cr (0.1 at%) codoped Nd (1.0 at%):YAG transparent ceramic rod (Konoshima Chemical Co. Ltd.) shown in the abscissa at the bottom using the same  $\mu$ SPL system shown in Fig. 10.25. An OC of a curvature radius = 100 mm was used. The input solar power into the OAP is also indicated in the abscissa at the top. The maximum input solar power into the OAP was 3.61 W, which corresponds to direct solar radiation of  $792 \text{ W/m}^2$ . Passing through the preposing optical system of the total transmittance of 71.5 %, the maximum input solar power into the rod was 2.59 W. The threshold power at the end facet of the rod was 1.56 W, which was lower than that in Fig. 10.28. Dividing the value by the area of the focused size,  $\pi r_s^2$  of  $1.58 \times 10^{-7} \text{ m}^2$ , threshold power density of  $9.87 \text{ MW/m}^2$  could be obtained. The slope efficiency and the total efficiency against the input solar power into the rod were 2.6 % and 1.0 %, respectively. The external slope efficiency and the external solar energy conversion efficiency against the input solar power at the OAP were 1.8 % and 0.73 %, respectively.

The effects of different OC curvature radii, 500 and 1000 mm, were also examined. Further, two quadrangular-prism-shaped transparent ceramic rods of  $1 \times 1 \times 10$  mm of Cr 0.1 at% codoped Nd 1 % doped YAG and Cr 0.4 at% codoped Nd 2 % doped YAG supplied by World Lab. Co. Ltd, were also tested in the same  $\mu$ SPL system shown in Fig. 10.25. Table 10.1 summarizes the results. Experiment (a) shown in Fig. 10.29 is the best data among the five results.

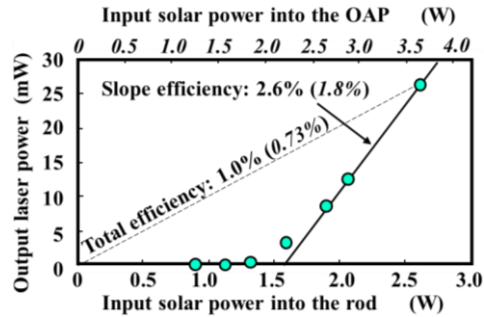


**Fig. 10.29.** Output laser power of the  $\mu$ SPL as a function of the input solar power into the rod. The input laser powers into the OAP are indicated with italic letters to show the real solar energy conversion efficiency.

**Table 10.1.** Slope efficiencies and threshold powers in the different experimental setups.

Exp. No.	Size (mm)	Dopants	Radius of OC (mm)	Slope efficiency (%)	Threshold power (W)
(a)	$\varnothing 1 \times 10$	Cr0.1 %, Nd1 %	100	2.60	1.56
(b)	$\varnothing 1 \times 10$	Cr0.1 %, Nd1 %	500	1.68	1.26
(c)	$\varnothing 1 \times 10$	Cr0.1 %, Nd1 %	1000	1.73	1.38
(d)	$1 \times 1 \times 10$	Cr0.1 %, Nd1 %	100	0.78	2.26
(e)	$1 \times 1 \times 10$	Cr0.4 %, Nd2 %	100	1.40	1.20

## 10.6. Continuous Oscillation of $\mu$ SPL for Over 6.5 Hours Tracking the Sun

Using the same condition as Experiment (a) in Table 10.1, continuous oscillation was tried outdoors tracking the Sun. Instead of the altazimuth (Vixen SKYPOD) in Fig. 10.27, a commercially available automatic equatorial mounting (VIXEN SXD2) with a tripod was employed seeking perfect solar tracking. The system was set at the roof terrace of Building 3 of Faculty of Engineering, Nagoya University located at latitude  $35^{\circ}10'N$  north and longitude  $136^{\circ}58'E$ , Nagoya, Japan. A continuous oscillation experiment was performed on a clear weather day, Wednesday, August 9<sup>th</sup>, 2017. The  $\mu$ SPL experimental rig is pictured in Fig. 10.30. Output power of the  $\mu$ SPL was measured with a power meter sensor every 0.3 seconds and the measured value was stored in the memory, coinstantaneously. A pyrheliometer shown in Fig. 10.14 and a solar telescope were fabricated and mounted on the same equatorial mounting with the  $\mu$ SPL and tracked the Sun simultaneously. The power of the direct solar radiation in 5 degrees in view angle and in the wavelength range of 190 nm to 25  $\mu$ m captured with an aperture and a pinhole was measured with a THOLABS S302C thermal power meter sensor attached to the pyrheliometer. The THOLABS S302C power meter sensor had been calibrated with an EKO INSTRUMENTS MS-53 (ISO 9060 First Class Pyrheliometer) that provided the value of the direct solar radiation in terms of  $W/m^2$ . These data were measured as well as recorded in memory every 0.3 seconds. The inset at the lower left in Fig. 10.30 is an image of the

Sun on a computer display monitored by the solar telescope using a video-capturing attachment. As reference, global solar irradiance was measured with a digital illuminometer. After adjustment of the direction of the  $\mu$ SPL roughly using the image of the Sun on the PC display monitored by the solar telescope, precise adjustment of screws fixing the  $\mu$ SPL onto the mounting provided a sudden rise in the output power of the  $\mu$ SPL from several  $\mu$ W to several mW at 10:50, indicating that laser oscillation was taking place. After start of the  $\mu$ SPL oscillation, the solar telescope was replaced by the pyr heliometer, and the measurement of the direct solar radiation was performed in parallel with the measurement of the output power of the  $\mu$ SPL.

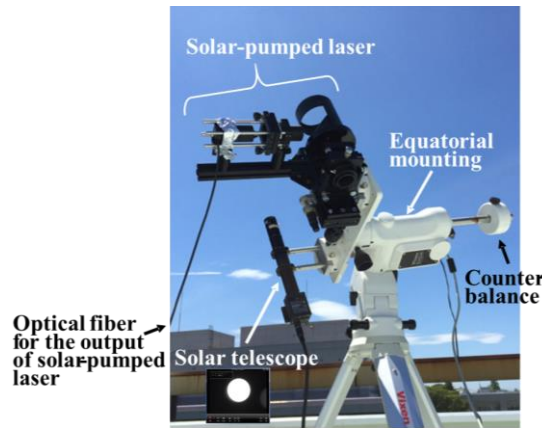


**Fig. 10.30.**  $\mu$ SPL system tracking the Sun automatically on an equatorial mounting (VIXEN SXD2). The inset figure in the lower left is an image of the Sun on a PC display monitored by the solar telescope using a video-capturing attachment for a rough adjustment of direction of  $\mu$ SPL toward the Sun.

Fig. 10.31 shows the variation in  $\mu$ SPL output power as a function of time in the lower blue line. The variation of the direct solar radiation in terms of  $\text{kW/m}^2$  is also shown in the upper red line. For reference, the global solar irradiances at three different clock times indicated on the illuminometer—109000 lx at 11:08, 114000 lx at 11:59, and 43600 lx – at 16:48 are also shown at the upper side of the figure. Simultaneous instantaneous falls both in the  $\mu$ SPL output and in the direct solar radiation around 13:22-13:36 and 17:17 were caused by passing clouds. With occasional manual readjustments of the equatorial mounting such as at 11:10, 11:23, 11:33, 11:43, 11:52, 12:00, 12:25, 12:55, 13:48, 14:46, 15:16, 15:37, 16:11, 16:29, and 17:00, the output power recovered 2-3 mW. Especially the readjustment at 12:00 provided an approximately 4.5 mW increase in the  $\mu$ SPL output. The maximum direct solar radiation over  $898 \text{ W/m}^2$  took place between 12:00 and 13:00 in which the  $\mu$ SPL output also reached its maximum of around 12 mW. The  $\mu$ SPL output kept going over 10 mW until 14:30. After continuous decrease, the output power of the  $\mu$ SPL suddenly fell from 0.2 mW to 0.0017 mW between 17:34 and 17:35, although instantaneous oscillations were observed several times beyond 17:35. After 17:35 until 17:51, almost all the measured output powers were around 0.0017 mW. Therefore, it is considered that the  $\mu$ SPL stopped continuous oscillation between 17:34 and 17:35. It was

positive outcome that the  $\mu$ SPL kept continuous oscillation even if the direct solar radiation was lower than  $550 \text{ W/m}^2$  around 17:30, that is, 61 % of the maximum value. This indicates the possibility of continuous oscillation for 11 hours from 6:30-17:30, which is considerably longer than our expectation and favorable for solar energy utilization. Fig. 10.32 shows a plot of these synchronous 47012 data sets, that is, a plot of  $\mu$ SPL output against the incident direct sunlight power at the entrance of the OAP. The distribution of the data clearly shows the existence of a threshold incident direct sunlight power around  $1.47 \text{ W}$  ( $2.05 \text{ W}$ ) for laser oscillation and a linear increase in  $\mu$ SPL output power with incident direct sunlight power larger than  $1.47 \text{ W}$  ( $2.05 \text{ W}$ ). This plot was realized because the measurement and the data acquisition of  $\mu$ SPL output power were continued beyond 17:30 after the oscillation stopped because of shadowing of sunlight by clouds spreading flat to the western horizon. A more detailed inspection of Fig. 10.32 reveals existence of two straight lines: one is in the region under  $2.7 \text{ W}$  of the total incident power (under  $5 \text{ mW}$  of the  $\mu$ SPL output), and the other is in the region over  $2.7 \text{ W}$  of that (over  $5 \text{ mW}$  of the  $\mu$ SPL output), with an inflection point around  $2.7 \text{ W}$ . Since the  $\mu$ SPL output was over  $5 \text{ mW}$  in the major day time before 16:30 in this experiment as shown in Fig. 10.31, we estimated the slope efficiency (external slope efficiency) to be 1.15 % (0.82 %) from the straight line over  $2.7 \text{ W}$ . The slope efficiency based on the straight line below  $2.7 \text{ W}$  is discussed next using the inset figure in Fig. 10.32.

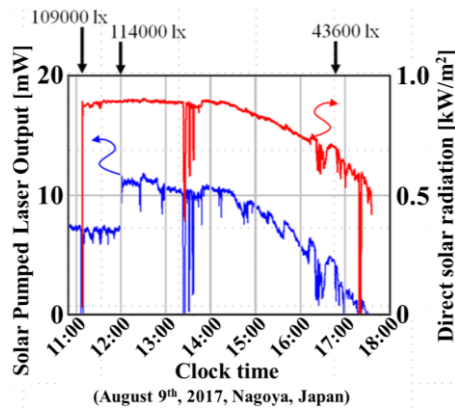


**Fig. 10.31.** Variation of  $\mu$ SPL output power as a function of time with an occasional manual readjustment of equatorial mount during automatic solar tracking. Variation of the direct solar radiation in terms of  $\text{kW/m}^2$  measured by a pyrliometer is also shown. For reference, the measured global solar irradiance in terms of lx at three different clock times are shown at the upper side.

To understand whether the red shift as the afternoon grew late (as displayed in Figs. 10.12 and 10.15) influenced the oscillation properties of the  $\mu$ SPL or not, a replot is shown in the inset figure in Fig. 10.32 in which the 8000 data points measured in the last 40 minutes after 16:50 are indicated using red markers while the others are indicated using gray markers. Those red-marked data were measured under insolation with the spectrum almost equal to or more redshifted than that at 16:50 indicated in Fig. 10.15. The distribution of

the red markers is consistent with the second straight line below 2.7 W of the total incident power described above. The slope efficiency deduced from this second straight line is evidently lower than that deduced from the total data in the main figure. To compare the slope efficiency quantitatively, the slope efficiency (external slope efficiency) of 1.08 % (0.77 %) was deduced from the second straight line while that deduced from the first line was 1.15 % (0.82 %). The two straight lines do not positively indicate the existence of two different threshold incident direct sunlight powers for laser oscillation but rather the same one around 1.47 W (2.05 W).

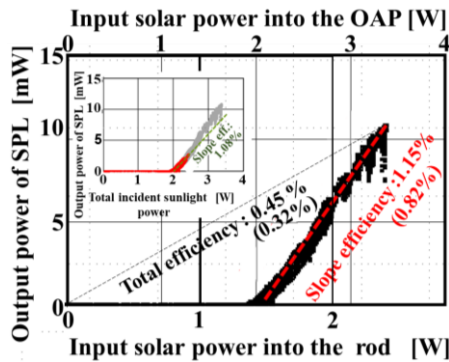


**Fig. 10.32.** Plots of  $\mu$ SPL output power against incident direct sunlight power at the entrance of the OAP using the 47012 data sets from those shown in Fig. 10.31. The inset at the upper left is a replot emphasizing the 8000 data points that correspond to the last 40 minutes after 16:50 indicated using red markers while others are marked using gray markers.

The results in Figs. 10.29 and 10.32 were obtained employing the same laser rod together with the same solar concentrator of  $\varnothing 76.2$  mm caliber OAP. Although there is no remarkable difference in the threshold power between the two experiments, the slope efficiency and the total efficiency are more than halved in the result in Fig. 10.32 in comparison with that in Fig. 10.29. Almost two years had passed when the experiment in Fig. 10.32 was performed since the experiment in Fig. 10.29. Between the two experiments, repeated test experiments were done using the same laser rod. It is known that there is a degradation of Nd:YAG transparent ceramics, known as solarization, which is thought to be caused by sunlight exposure. However, the origin of solarization has not been clarified yet because the degradation is difficult to detect via instrumental analyses. Although a UV filter (Kenko Tokina Zeta UV L41) was always set at the entrance of the OAP in our experiments, degradation of the laser rod is a possible cause of the decrease in the efficiencies. The prevention of degradation of the laser rod will be one of key challenges before commercial adoption of SPLs.

In previous study [23], a water-cooled Nd:YAG crystal rod was pumped with a  $\varnothing 61$  cm, solar tracking, equatorial mount solar collector to give 1 W of continuous wave (CW) laser output. Although the study claims that “Operation over many hours was obtained with no evidence of reduction of output,” no evidential data of continuous oscillation was provided. An evidential record of continuous oscillation for 11 min was reported employing a water-cooled Nd:YAG rod and a 10 m aperture solar collector [42], in which

tracking error was corrected manually 8-10 times during this 11 min continuous operation. A record of 60 sec stable continuous oscillation was also reported employing a water-cooled Nd:YAG ceramic rod and 2 m × 2 m Fresnel lens to generate 110 W CW laser output [63]. More recently, records of continuous oscillation of solar-pumped 1064 nm laser emission with a simple Gaussian intensity distribution around the center axis of the beam (TEM<sub>00</sub>-mode) for 4 minutes have been reported [99]. Therefore, the result shown in Fig. 10.31 is a record long continuous laser oscillation of SPL tracking the Sun [100]. This is an indispensable experimental step if SPLs are to be applied to terrestrial solar energy utilization.

### 10.7. Effect of Cr Content in a Cr-Codoped Nd:YAG Transparent Ceramic Laser Rod for $\mu$ SPLs

Direct experimental comparison of the effect of Cr, Nd:YAG ceramic LMs with different Cr contents on the SPL output was performed. Quadrangular-prism-shaped LMs of transparent Cr-codoped Nd:YAG ceramics ( $1 \times 1 \times 10$  mm, and  $1 \times 1 \times 20$  mm) were prepared with Cr contents of 0.0, 0.4, 0.7, and 1.0 at% with a fixed Nd content of 1.0 at%. These LMs were fabricated by World Lab. Co. Ltd., Atsuta, Nagoya, Japan [45, 46]. The  $\mu$ SPL system is the same as shown in Figs. 10.25 and 10.26. Fig. 10.33 shows a photograph of the prepared LMs; the greenish color is attributed to Cr<sup>3+</sup>. The end facet of an LM was coated with a high-reflectivity (HR) coating consisting of a multilayered thin film optical filter with 95 % transmittance for focused sunlight coming from the OAP and a reflectivity ( $R_{HR}$ ) of 99.95 % for the 1064 nm monochromatic light emitted by Nd<sup>3+</sup> in the LM. The other side of the LM was coated with a broadband antireflection (BBAR) coating consisting of a multilayered thin film optical filter with more than 95 % transmittance of sunlight with wavelengths between 780 and 1064 nm and almost 100 % transmittance of 1064 nm monochromatic light. The laser cavity contained the HR coating on the end facet of the LM and the concave mirror of OC with a curvature radius  $r$  of 100 mm and a diameter of 10 mm.

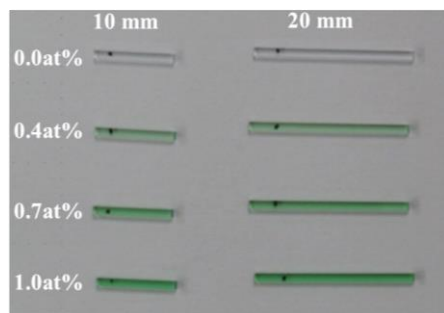


**Fig. 10.33.** Photograph of the prepared Cr-doped Nd (1.0 at%): YAG rods. Cr content is indicated on the left. Length of the rod is indicated at the top. The black points near the left ends of the rods indicate that the left end facets of the rods were coated with HR coatings, whereas the right end facets were coated with BBAR coatings.

An outdoor  $\mu$ SPL oscillation experiment was performed on the same location as shown in Figs. 10.27 and 10.30. Figs. 10.34(a) and (b) show plots of measured  $\mu$ SPL outputs against the incident direct sunlight power into the OAP ( $I_{\text{OAP}}$ ) for the 10 mm and 20 mm LMs, respectively [101]. The incident sunlight power at the edge of LM,  $I_{\text{LM}}$ , is 71.5 % of  $I_{\text{OAP}}$  in this light collection system employing the OAP, as was reported in Section 10.3. Here, the OC had a reflectivity  $R_c$  of 99 % for laser emission (1064 nm). For both the LMs, the output power of the  $\mu$ SPL took the maximum at a Cr content of 0.4 at%. The output power at a Cr content of 0.4 at% was approximately 8.5 times that at a Cr content of 0.0 at%. The output power decreased as the Cr content increased beyond 0.4 at%. At a Cr content of 1.0 at% for the 20 mm LM, the output power was even lower than that for the LM without Cr doping. It is not easy to define the portion of linear increase of  $\mu$ SPL output with  $I_{\text{OAP}}$ . However, we can compare the threshold input powers and slope efficiencies of the LMs using the values of the  $I_{\text{OAP}}$  intercept  $I_{\text{eth}}$  with the line connecting the point of the highest  $\mu$ SPL output and the point of the second highest  $\mu$ SPL output obtained in this experiment for each Cr content and the values of the corresponding slope  $\eta_{\text{slope}}$ . Table 10.2 lists the obtained values of  $I_{\text{eth}}$  and  $\eta_{\text{slope}}$ .

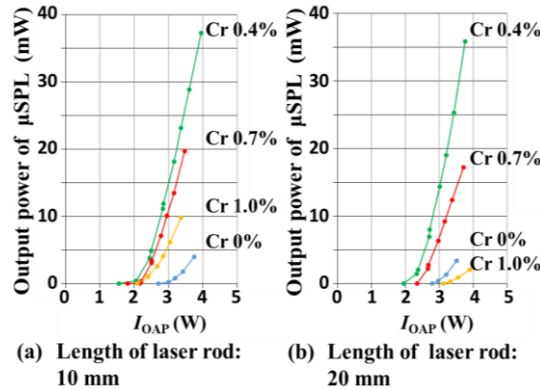


**Fig. 10.34.** Plots of measured  $\mu$ SPL output power against the incident direct sunlight power into the OAP,  $I_{\text{OAP}}$  for (a) 10 mm and (b) 20 mm transparent Cr-doped Nd (1.0 at%) YAG LMs with different Cr contents.

In addition to the outdoor laser oscillation experiments pumped by direct sunlight, laser oscillation experiments in which  $\text{Nd}^{3+}$  was pumped directly using an 808 nm LD were performed in an indoor laboratory. To couple the 808 nm excitation beam, a long-working-distance objective lens (focal length = 10 mm) was used. Here, OCs of  $r = 100$  mm, diameter = 20 mm, and reflectivity  $R_c = 90$  %, 95 %, and 99 % for laser emission (1064 nm) were employed. Fig. 10.35 (a) shows a typical oscillation property of the 10 mm LM of Cr (0.4 at%), Nd (1.0 at%):YAG ceramic obtained in the laser oscillation experiments by pumping  $\text{Nd}^{3+}$  directly using an 808 nm LD in an indoor laboratory. Here, an OC with a reflectivity  $R_c$  of 95 % for the laser emission (1064 nm) was employed. To evaluate the round-trip loss  $\delta_{808}$  in the laser cavity, the oscillation properties were also obtained using OCs with  $R_c$  of 90 % and 99 %. Fig. 10.35 (b) shows a plot of  $I_{\text{eth}}(808)$  for the three measurements at different values of  $R_c$  against  $\log_e R_c$ . The

extrapolation of a line determined by least-square fitting of the three data points intercepts the horizontal  $\log_e R_c$  axis at -0.026. Therefore,  $\delta_{808}$  was found to be 0.026 [102]. Similarly, the  $\delta_{808}$  values of the eight LMs were obtained and are listed in Table 10.2, together with the  $\eta_{\text{slope}(808)}$  and  $I_{\text{eth}(808)}$  values obtained in these indoor experiments.

The results in Table 10.2 show that  $\delta_{808}$  increased with increasing Cr content. The value of  $\eta_{\text{slope}(808)}$  did not increase as dramatically as  $\eta_{\text{slope}}$  but did show a slight increase between 0.0 at% Cr and 0.4 at% Cr. At Cr contents exceeding 0.4 at%,  $\eta_{\text{slope}(808)}$  decreased gradually in both the 10 mm and 20 mm LMs. The increase in  $I_{\text{eth}(808)}$  was like that of  $\delta_{808}$  for both the 10 mm and 20 mm LMs. These results clearly show that the presence of  $\text{Cr}^{3+}$  does not affect the oscillation process because of direct excitation of  $\text{Nd}^{3+}$  by the LD. In contrast, for both the 10 and 20 mm LMs,  $I_{\text{eth}}$  showed a steep decrease between 0.0 at% Cr and 0.4 at% Cr, reaching a minimum between 0.4 at% Cr and 0.7 at% Cr and increased again toward 1.0 at% Cr. According to Eq. (10.8), the increase in Cr content is thought to contribute to the increase in  $I_{\text{eth}}$  via the increase in  $\delta$ . However, the increase in the Cr content also contribute to the decrease in  $I_{\text{eth}}$  via the increase in  $\eta_{\text{abs}}$  in Eq. (10.8). The minimum value of  $I_{\text{eth}}$  at a Cr content of 0.4 at% is attributed to these two conflicting contributions. Because the increase in  $I_{\text{eth}}$  was observed even at low Cr contents between 0.4 % and 0.7 %, the possible effect of concentration quenching is thought to have little effect on the increase in  $I_{\text{eth}}$  in this experiment. Recall that  $\eta_{\text{slope}}$  increased dramatically between 0.0 at% Cr and 0.4 at% Cr and decreased gradually beyond 0.4 at% Cr. The maximum  $\eta_{\text{slope}}$  at 0.4 at% Cr was 2.43 % for the 10 mm LM and 3.19 % for the 20 mm LM. These values are converted to 3.40 % and 4.46 %, respectively, if the  $\mu\text{SPL}$  output is plotted against not  $I_{\text{OAP}}$  but  $I_{\text{LM}}$ . These values are competitive with the current state-of-the-art values [60].

**Table 10.2.** Measured values:  $I_{\text{eth}}$  and  $\eta_{\text{slope}}$ - of the eight LMs obtained outdoors under sunlight, and the round-trip loss  $L_{808}$ ,  $I_{\text{eth}(808)}$  and  $\eta_{\text{slope}(808)}$  obtained indoors under 808 nm LD pumping.

$\text{Cr}^{3+}$ (at%)	10 mm LM					20 mm LM				
	$I_{\text{eth}}$ (W)	$\eta_{\text{slope}}$ (%)	$\delta_{808}$ (%)	$\eta_{\text{slope}(808)}$ (%)	$I_{\text{eth}(808)}$ (mW)	$I_{\text{eth}}$ (W)	$\eta_{\text{slope}}$ (%)	$\delta_{808}$ (%)	$\eta_{\text{slope}(808)}$ (%)	$I_{\text{eth}(808)}$ (mW)
0	2.98	0.36	2.5	47.2	45.5	3.03	0.67	2.8	37.9	58.6
0.4	2.41	2.43	2.6	49.2	50.6	2.64	3.19	2.6	43.5	59.7
0.7	2.49	2.00	3.0	37.4	70.9	2.52	1.44	3.8	32.3	79.3
1	2.52	1.15	4.5	26.6	85.3	3.26	0.34	5.8	18.1	93.8

These results indicate that Cr doping is effective for decreasing  $I_{\text{th}}$  and increasing  $\eta_{\text{slope}}$  because of increased optical absorption by  $\text{Cr}^{3+}$ . Although it was demonstrated that Cr doping increases  $\delta_{808}$ , it was also found that the increase in  $\delta_{808}$  between 0.0 at% Cr and 0.4 at% Cr was small compared with the increase between 0.4 at% Cr and 1.0 at% Cr. Therefore, the  $\mu\text{SPL}$  output showed an outstanding maximum at 0.4 at% Cr, because it is determined by competition between the positive effect of increased energy transfer from  $\text{Cr}^{3+}$  to  $\text{Nd}^{3+}$  and the negative effect of increased  $\delta$  with increase in Cr content. It appears that these conditions were the same for both 10 and 20 mm LMs.

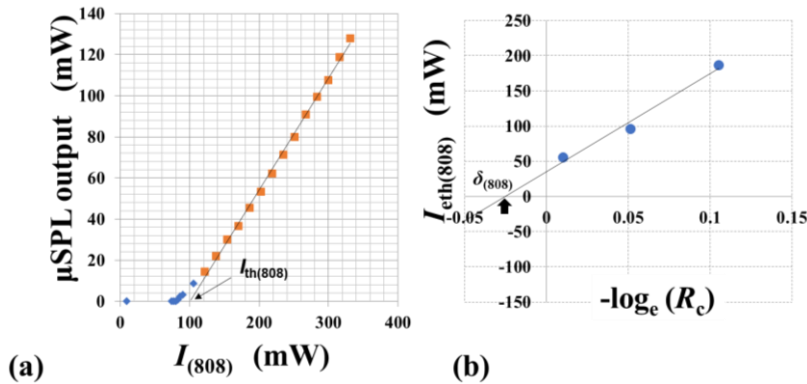


**Fig. 10.35.** (a) Plots of  $\mu\text{SPL}$  output against the incident 808 nm laser power  $I_{(808)}$  into the 10 mm LM of Cr (0.4 at%),Nd (1.0 at%):YAG, where an OC with  $r$  of 100 mm, a diameter of 20 mm, and a reflectivity  $R_c$  of 95 % at 1064 nm was employed. (b) Plot of  $I_{\text{eth}(808)}$  for  $R_c$  of 90 %, 95 %, and 99 % against  $\log_e R_c$ .

## 10.8. For Improvement of Mode-matching Efficiency

In this work, it has been established that sunlight can be concentrated to exceed  $I_{\text{eth}}$  at the end facet of LMs by using OAPs. However, this raises a serious issue, known as the “mode-matching problem,” which means that there is sufficient overlap between the laser mode profile and the propagation mode of the pumping light is difficult to achieve. Fig. 10.36 schematically shows how the concentrated direct sunlight propagates in an LM. The thin, red cylindrical region stands for a simplified laser mode profile. The overlap is maximum when the length of the LM is small, that is, in the case of disk-shaped LM. With increase in the length of LM, the overlap decreases toward the constant value because the converged sunlight at the end facet of the LM diverges again in the LM. Pumping the region not overlapping with the laser mode does not contribute to the laser output but only leads to energy loss. In Figs. 10.16 and 10.24, several typical traces of light rays are indicated to show the image formations. Here, more detailed tracing of sunlight was performed using a commercially available simulation software ZEMAX. Fig. 10.37(a) shows the result for traces of sunlight reflected by an OAP and converged on an end facet of  $\varnothing 1 \times 10$  mm LM. Fig. 10.37(b) shows a distribution of the absorbed power of the pumping light propagating in the LM. The distribution reflects asymmetric nature of the converged light by OAP in the first 1 mm and extends widely in the LM, implying significant loss in the peripheral region out of the laser mode. Combining a laser cavity analysis software LASCAD, the output laser powers were simulated as a function of the input solar power into the rod assuming  $2.8 \times 10^{-19} \text{ cm}^2$  for  $\sigma(\lambda_L)$ , 230  $\mu\text{sec}$  for  $\tau$  [98], 0.02 for  $\delta$ , and 0.8 for  $\eta_{\text{QE}}$ . The results are shown in Fig. 10.38. The simulated results give a threshold power of 1.44 W and a slope efficiency of 2.8 % while the corresponding experimental values are 1.56 W and 2.6 %. Although the simulated results approximately reproduced the experimental results in Fig. 10.29, the slightly better threshold power and the slope efficiency imply  $\eta_{\text{QE}}$  lower than 0.8, thereby reflecting poor energy transfer efficiency from  $\text{Cr}^{3+}$  to  $\text{Nd}^{3+}$ . If the doping region in  $\varnothing 1 \times 10$  mm rod could be reduced,

for example, within  $\varnothing 0.4$  mm, 0.6 mm, or 0.8 mm as shown in Fig. 10.39(a), the absorption of the light would take place only within the doped region as shown in a simulated result in Fig. 10.39(b). Here, we call this structured rod shown in Fig. 10.39(a) as a composite rod. Simulated output laser powers plotted against the input solar power into the rods by ZEMAX and LASCAD shown in Fig. 10.39 (c) indicate a decrease in the threshold power with decrease in the diameters of the doped regions. This is possibly caused by the increase in mode-matching, that is, the decrease of the absorption out of the laser mode that does not contribute the laser output. However, reduction of the doped region less than  $\varnothing 0.8$  mm led to decrease in the slope efficiency, which is possibly caused by the decrease in the absorbed light in the laser mode region because of the excessive reduction in the doped region.

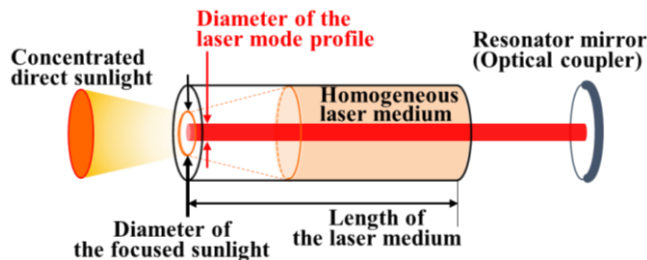


**Fig. 10.36.** Schematic representation of a laser mode profile and pumping light propagation in a laser medium.

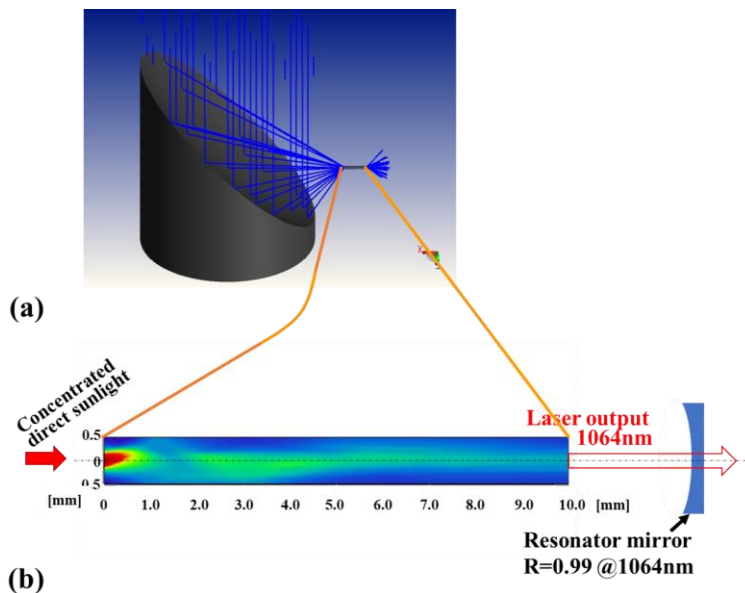


**Fig. 10.37.** (a) Ray tracing of the sunlight concentration onto  $\varnothing 1 \times 10$  mm, Cr (0.1 at%) codoped Nd (1.0 at%):YAG transparent ceramic rod by an OAP; (b) Absorbed power distribution in the laser medium (optical simulation code: ZEMAX).

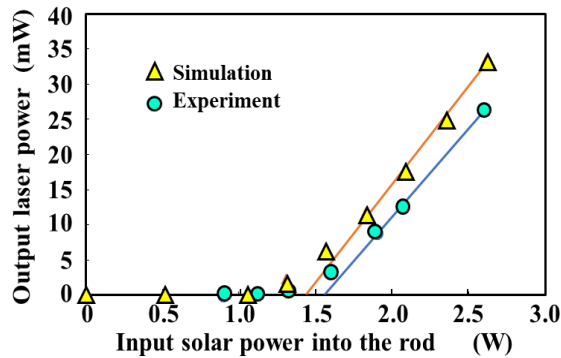


**Fig. 10.38.** Output laser power of the  $\mu$ SPL as a function of the input solar power into the rod simulated combining ZEMAX and LASCAD. The corresponding experimental data shown in Fig. 10.29 were also replotted for reference.

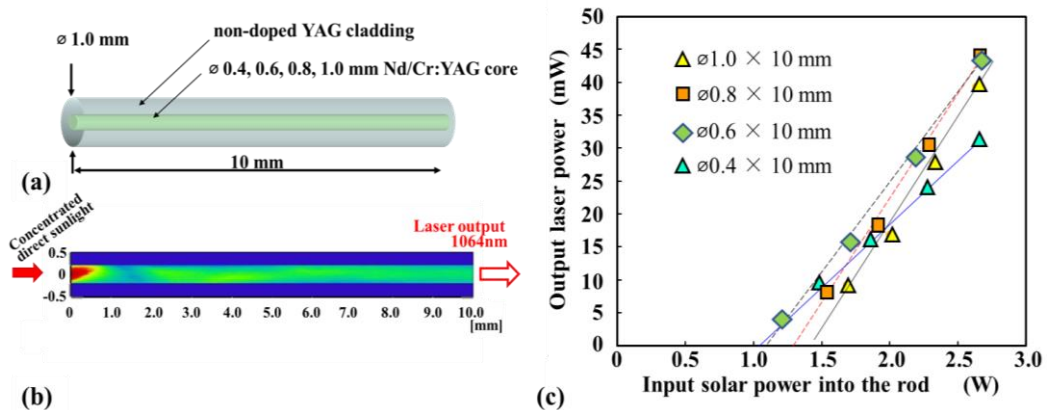


**Fig. 10.39.** Effects of reduction of the doped region in a YAG micro rod. (a) A schematic composite rod structure; (b) Absorbed power distribution in the composite rod simulated using ZEMAX; (c) Output laser power of the composite rod SPL as a function of the input solar power into the rod simulated combining ZEMAX and LASCAD.

Although the reduction in the doped region to form a composite rod is effective for improving mode-matching, the difference in the refractive indices between the core and the cladding causes another loss, that is, diffraction loss between the exit end facet of the rod and a resonator mirror as shown in Fig. 10.40 (a). By doping 5 at% non-absorbing Gd, the refractive index of the cladding was matched with that of core (Fig. 10.40 (c)), and the diffraction loss could be eliminated as shown in Fig. 10.40(b). For ease of production, quadrangular-prism-shaped composite rods in place of concentric cylinders, as shown in Fig. 10.39 (a), were chosen. Fig. 10.41 shows photographs of (a) a colorless Gd 5 at% doped YAG transparent ceramic LM, (b) a greenish Cr 0.4 at%, Nd 1 at% doped transparent ceramic LM, (c) a cross-sectional view of 2D composite LM, (d) a

cross-sectional view and part side view of a quadrangular-prism-shaped three-dimensional (3D) composite LM.

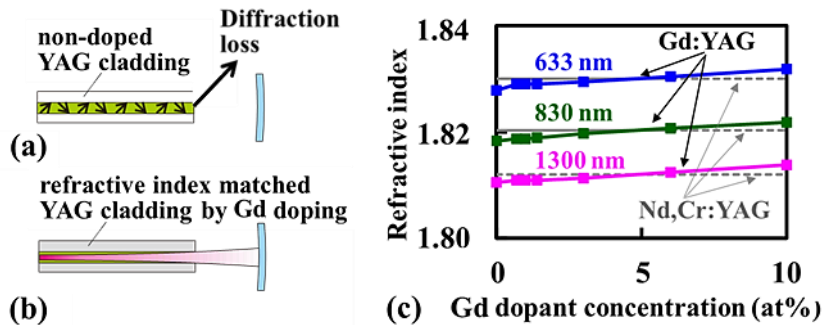


**Fig. 10.40.** Refractive index matching between the Cr, Nd: YAG core and the Cr, Nd non-doped YAG cladding by non-absorbing Gd in the cladding to reduce the diffraction loss between the exit end facet of the rod and a resonator mirror.

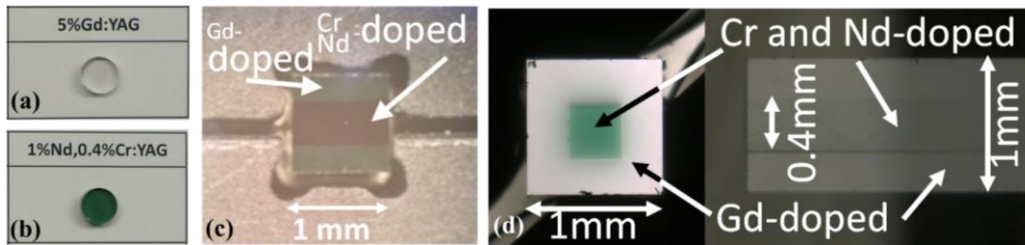


**Fig. 10.41.** Photographs of (a) a colorless Gd 5 at% doped YAG transparent ceramic LM, (b) a greenish Cr 0.4 at%, Nd 1 at% doped transparent ceramic LM, (c) a cross-sectional view of a quadrangular-prism-shaped two-dimensional(2D) composite LM, (d) a cross-sectional view, and a part of a side view of a quadrangular-prism-shaped three-dimensional(3D) composite LM.

Using a convergent monochromatic light of  $NA = 0.4$  formed from an 808 nm diode laser that directly excites  $Nd^{3+}$  ions (Fig. 10.42 (a)), preliminary evaluations of composites rods shown in Fig. 10.41 (c) and (d) were performed. The results shown in Fig. 10.42 (b) elucidate a lower threshold power and a higher slope efficiency for 2D composite rod in comparison with those for a conventional homogeneous rod, and even better results for 3D composite rod than that for 2D composite rod [103]. Although an experimental proof of the advantages of 3D composite rods by outdoor oscillation tracking the Sun remains a challenge for the future, the slope efficiency in a 3D composite rod with a  $0.4 \times 0.4$  mm core in a  $1 \times 1 \times 10$  mm LM under white light pumping is simulated to be 18 %, as shown in Fig. 10.43 whereas that in a 2D composite rod is 3.1 % and that in a homogeneous (conventional) rod is 1.3 %. Therefore, more precise adjustment of core size may bring better mode-matching and better efficiencies.

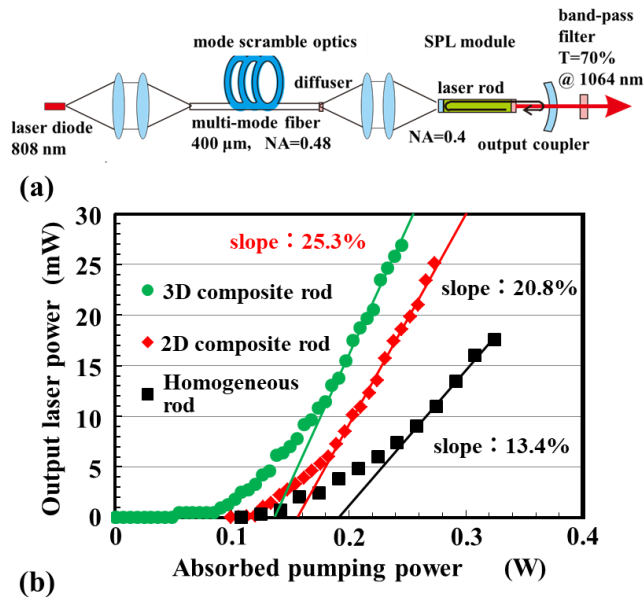


**Fig. 10.42.** (a) Monochromatic convergent beam optics for preliminary evaluation of 2D and 3D rods; (b) Results of comparative evaluations of a conventional homogeneous rod, 2D composite rod, and 3D composite rod.

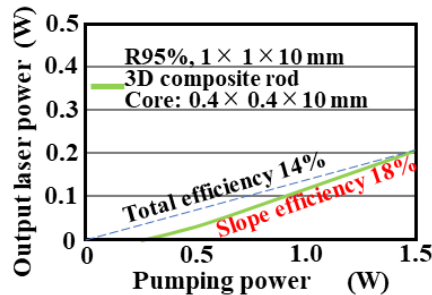


**Fig. 10.43.** Simulated oscillation property of a 3D composite rod under white light pumping.

### 10.9. Evaluation of Energy Transfer Efficiency from $\text{Cr}^{3+}$ to $\text{Nd}^{3+}$ in $\mu\text{SPL}$ in Outdoor Operation

As shown in Fig. 10.34, Cr codoping is effective in increasing the output laser power at 0.4 at% in comparison with no codoping. However, in the cases of codoping of 0.7 at% Cr and 1 at% Cr, the demerit of the increase in the round-trip loss  $\delta$  offset the merit and the output laser power decreased. There is a previous study that reports that the performance of Cr, Nd:YAG ceramics was inferior to that of undoped Nd:YAG crystals in an SPL where a  $3 \times 9 \times 100$  mm transparent Cr, Nd:YAG ceramic LM was tested in a specially designed SPL employing end-pumping and side-pumping simultaneously using

a liquid light-guide lens [91]. The reason suggested was as follows: (1) Cr codoping increased the scattering coefficient of transparent Nd:YAG ceramic rods, (2) the increase in the scattering coefficient of the rods leads to an increase in the round-trip loss  $\delta$  in the laser cavity, (3) the increase in  $\delta$  leads to a decrease in  $\eta_{\text{slope}}$ , (4) the decrease in  $\eta_{\text{slope}}$  offsets the advantage of the decrease in the saturation gain caused by increased optical absorption by  $\text{Cr}^{3+}$  followed by energy transfer from  $\text{Cr}^{3+}$  to  $\text{Nd}^{3+}$ . This agrees with the results observed in Fig. 10.34. Since then, undoped transparent Nd:YAG LMs have been used in SPLs [58, 59]. However, using  $\varnothing 4.5 \text{ mm} \times 35 \text{ mm}$  Cr (0.1 at%)-doped Nd (1.0 at%):YAG ceramic rod, the same authors recently reported a slope efficiency 1.28 times their own previous record [58, 60]. Therefore, the advantage of using transparent Cr, Nd:YAG ceramic LMs instead of Nd:YAG single-crystal LMs in SPLs is not conclusive.

It was also suggested from the simulated result in Fig. 10.38 that  $\eta_{\text{QE}}$  might be less than 0.8, reflecting poor energy transfer efficiency from  $\text{Cr}^{3+}$  to  $\text{Nd}^{3+}$ . Fig. 10.44 schematically shows the energy diagram of  $\text{Cr}^{3+}$  and  $\text{Nd}^{3+}$  in YAG crystal including energy transfer process from  $\text{Cr}^{3+}$  to  $\text{Nd}^{3+}$ .  $\text{Cr}^{3+}$  ions excited by sunlight relax to  ${}^4\text{T}_2$  state or  ${}^2\text{E}$  state. Through the transition of  $\text{Cr}^{3+}$  ions from these excited states ( ${}^4\text{T}_2$  or  ${}^2\text{E}$ ) to the ground state ( ${}^4\text{A}_2$ ), it is considered that energy is transferred from  $\text{Cr}^{3+}$  to  $\text{Nd}^{3+}$  ions to put  $\text{Nd}^{3+}$  ions eventually into the metastable excited state  ${}^4\text{F}_{3/2}$ . It is considered that this process increases the pumping efficiency and decreases the threshold power for laser oscillation.

However, the direct excitation of  $\text{Nd}^{3+}$  ions by sunlight may increase the number of  $\text{Nd}^{3+}$  ions at the metastable excited state  ${}^4\text{F}_{3/2}$  so much that  $\text{Cr}^{3+}$  ions excited by sunlight cannot find enough  $\text{Nd}^{3+}$  ions at the ground state to which energy is transferred. This may cause poor energy transfer efficiency from  $\text{Cr}^{3+}$  to  $\text{Nd}^{3+}$ . To simulate this situation experimentally, laser oscillation experiments with simultaneous direct excitation of  $\text{Nd}^{3+}$  by an 808 nm laser and the direct excitation of  $\text{Cr}^{3+}$  by 561 nm that does not excite  $\text{Nd}^{3+}$  directly were performed as shown in Fig. 10.45 (a). Fig. 10.45 (b) shows output laser powers as a function of 808 nm pumping power in cases with and without 50 mW pumping at 561 nm. With 50 mW pumping at 561 nm, the output laser power increased in comparison with the case without 50 mW pumping at 561 nm. The increment can be attributed to the Cr to Nd energy transfer. Fig. 10.45(c) shows the decrease in the threshold power with increase in the input 561 nm power. From these results, the energy transfer efficiency was estimated to be 65.3 % [97].

A more realistic approach to access the Cr to Nd energy transfer efficiency was also tried using natural sunlight pumping outdoors. For the samples, Cr-codoped Nd (1.0 at%):YAG transparent ceramic LMs of  $1 \times 1 \times 10 \text{ mm}$  in size with Cr contents of 0.0 at%, 0.4 at%, 0.7 at%, and 1.0 at% shown in Fig. 10.33 were used again. Apart from the measurement of the stimulated emission, as shown in Fig. 10.25, the spontaneous emission spectra by sunlight excitation were also measured in a similar geometry as shown in Fig. 10.46 (a). Figs. 10.46 (b) and (c) show measured spontaneous emission spectra in the cases of sunlight intensity of 1.12 W and 3.07 W, respectively. Using the decrease in the threshold power caused by the energy transfer from  $\text{Cr}^{3+}$  ions to  $\text{Nd}^{3+}$  ions, the values of  $\text{Cr}^{3+}$  to  $\text{Nd}^{3+}$  energy transfer efficiency  $\eta_{\text{Cr} \rightarrow \text{Nd}}$  were estimated as shown in Fig. 10.47 [104]. In the

figure, the values estimated are not for  $\eta_{\text{Cr} \rightarrow \text{Nd}}$  but for  $(\eta_{\text{Cr}} / \eta_{\text{Nd}}) \cdot \eta_{\text{Cr} \rightarrow \text{Nd}}$ . Here,  $\eta_{\text{Cr}}$  is the quantum efficiency of the formation of the excited  $\text{Cr}^{3+}$  ions in the energy level  ${}^2\text{E}$  and  ${}^4\text{T}_2$  from the number of absorbed photons by  $\text{Cr}^{3+}$  ions, and  $\eta_{\text{Nd}}$  is the quantum efficiency of the formation of the excited  $\text{Nd}^{3+}$  ions in the metastable energy level of  ${}^4\text{F}_{3/2}$  from the number of absorbed photons by  $\text{Nd}^{3+}$  ions. In other words,  $\eta_{\text{Cr}}$  stands for the efficiency of relaxation of the excited electrons in higher energy levels of  $\text{Cr}^{3+}$  to their  ${}^4\text{T}_2$  or  ${}^2\text{E}$  levels, and  $\eta_{\text{Nd}}$  stands for the efficiency of relaxation of the excited electrons in higher energy levels of  $\text{Nd}^{3+}$  to the metastable  ${}^4\text{F}_{3/2}$  levels. The ratio  $\gamma (= \eta_{\text{Cr}} / \eta_{\text{Nd}})$  is not known. For the first-order approximation,  $\gamma$  can be assumed to be unity because both  $\eta_{\text{Cr}}$  and  $\eta_{\text{Nd}}$  represent similar properties of the isolated metal ions doped in YAG ceramics. For the second-order approximation,  $\gamma$  can be assumed to be a value slightly less than unity,  $\gamma \lesssim 1$ . Because the energy levels of rare-earth ions such as  $\text{Nd}^{3+}$  are not significantly influenced by the surrounding electronic structure of YAG matrix atoms,  $\eta_{\text{Nd}}$  is considered to be higher than  $\eta_{\text{Cr}}$  of a transition metal ion,  $\text{Cr}^{3+}$ . Since  $\gamma$ , which is nearly equal to unity, does not majorly influence the present discussion, the values listed in Fig. 10.47 are deemed to represent  $\eta_{\text{Cr} \rightarrow \text{Nd}}$ . When  $I_{\text{OAP}}$  was increased to 3.07 W,  $\eta_{\text{Cr} \rightarrow \text{Nd}}$  in spontaneous emissions decreased to  $0.675\gamma$  (0.4 at%),  $0.623\gamma$  (0.7 at%), and  $0.625\gamma$  (1.0 at%). In stimulated emissions,  $\eta_{\text{Cr} \rightarrow \text{Nd}}$  further decreased to  $0.448\gamma$  (0.4 at%),  $0.213\gamma$  (0.7 at%), and  $0.166\gamma$  (1.0 at%). The decrease in  $\eta_{\text{Cr} \rightarrow \text{Nd}}$  in the increased  $I_{\text{OAP}}$  in spontaneous emissions, and further decrease in  $\eta_{\text{Cr} \rightarrow \text{Nd}}$  in stimulated emissions may be attributed to the fact that the energy of the  $\text{Cr}^{3+}$  ions excited by sunlight cannot transfer to  $\text{Nd}^{3+}$  ions because the number of  $\text{Nd}^{3+}$  ions directly excited by sunlight and already occupying the metastable excited state,  ${}^4\text{F}_{3/2}$ , increased with increasing  $I_{\text{OAP}}$  in spontaneous emissions, and more seriously so in the population inversion in stimulated emissions. As for the dependence on the Cr content, the highest values of  $\eta_{\text{Cr} \rightarrow \text{Nd}}$  were obtained at 0.4 at% in line with the Cr content dependence of output powers of SPL shown in Fig. 10.34.

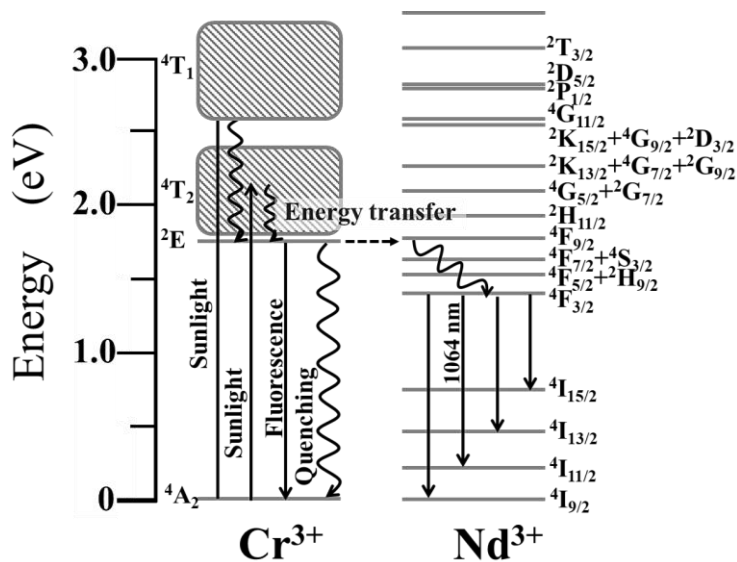
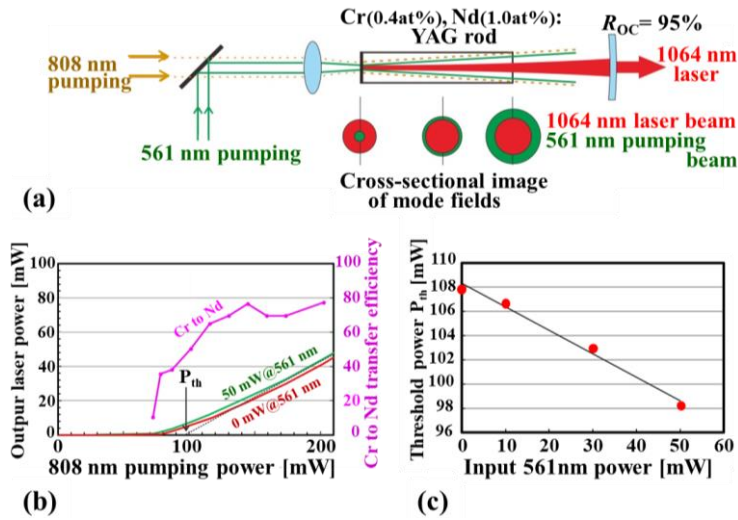
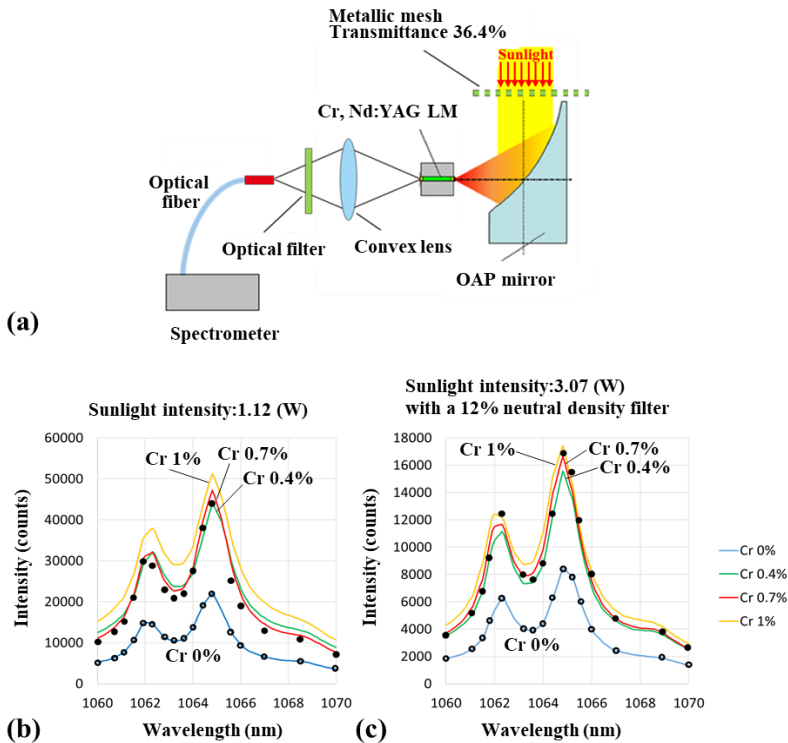


Fig. 10.44. Energy diagrams of  $\text{Cr}^{3+}$  and  $\text{Nd}^{3+}$  in YAG crystal under the sunlight excitation.



**Fig. 10.45.** (a) Experimental set-up of the Nd/Cr: YAG pumped by 808 nm and 561 nm lasers. (b) Laser output power property by two-wavelength pumping. (c) Laser oscillation threshold vs. the 561 nm pumping power.



**Fig. 10.46.** (a) Geometry to monitor solar-pumped spontaneous emission spectra. The optical filter transmits 70 % for  $\lambda$  of  $1064 \pm 2$  nm; (b) and (c) Measured spontaneous emission spectra in  $1060 \text{ nm} < \lambda < 1070 \text{ nm}$  at two different sunlight intensities of 1.12 W and 3.07 W, respectively.

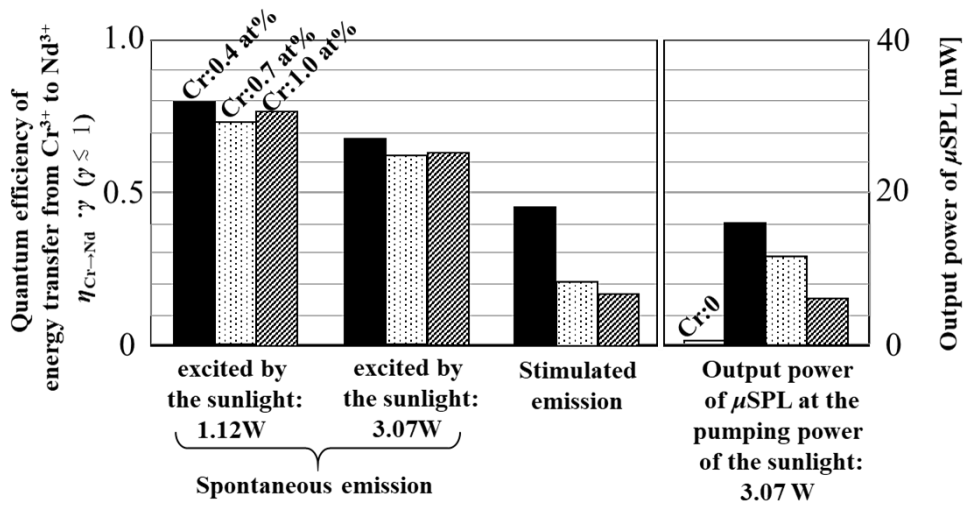


**Fig. 10.47.** Results of estimated  $\eta_{Cr \rightarrow Nd} \cdot \gamma$  displayed in bar charts to show (1) the dependence on the sunlight power in spontaneous emissions, (2) the difference between spontaneous emissions and stimulated emissions and (3) dependence on the Cr content. The Cr content dependence of the output power of  $\mu$ SPL at the pumping power of sunlight = 3.07 W is also attached.  $\gamma$  is the ratio  $\eta_{Cr}/\eta_{Nd} \lesssim 1$ ,  $\eta_{Cr}$  is the quantum efficiency of the formation of the excited  $Cr^{3+}$  ions in the energy level  ${}^2E$  and  ${}^4T_2$  from the number of absorbed photons by  $Cr^{3+}$  ions, and  $\eta_{Nd}$  is the quantum efficiency of the formation of the excited  $Nd^{3+}$  ions in the metastable energy level of  ${}^4F_{3/2}$  from the number of absorbed photons by  $Nd^{3+}$  ions.

Deeming  $\gamma$  to be unity, the values of  $\eta_{Cr \rightarrow Nd}$  obtained here in stimulated emissions are also much less than the values of  $\eta_{Cr \rightarrow Nd}$  in spontaneous emission. This indicates that Cr-codoped Nd:YAG is not an ideal LM. Improvement of  $\eta_{Cr \rightarrow Nd}$  is awaited for SPL. This is consistent with the motivation to develop novel LMs such as in Cr, Nd-doped garnet crystal families for SPLs in place of Cr, Nd:YAG [105, 106]. However, the advantages of Cr, Nd:YAG ceramics over novel LMs, such as grain sizes of a few micrometers resulting in suppressed scattering on the grain boundary, controllability of Cr and Nd concentrations, and thermal conductivity, have been still unchallenged. As briefly explained earlier, the problem of degradation due to solarization also needs to be solved in Cr-codoped Nd:YAG transparent ceramic LMs. To improve the spectral matching efficiency, we believe that it is promising to employ a vertical cavity surface emitting semiconductor laser (VECSEL) that absorbs all the solar photons with their energy larger than the bandgap of a semiconductor as a future challenge [107-109]. A VECSEL is essentially a disk-type LMs shown as an ideal form of LM in the top left corner in Fig. 10.6, in contrast to the current Nd:YAG rod-like micro LMs in our  $\mu$ SPL.

### 10.10. Coordinated Solar Tracking of an Array of $\mu$ SPLs to Harvest Larger Amount of Solar Energy

In contrast to a conventional SPL employing a large Fresnel lens or a large converging mirror with typical sizes or diameters in the range of 1-2 m and a water-cooled thick LM

of a typical size of  $\varnothing 10 \times 100$  mm [63-65], a  $\mu$ SPL can be mounted on a commercially available solar-tracking system for a telescope for amateur astronomers, as shown in Fig. 10.30, for all-day continuous lasing tracking the Sun only with natural air convection. This is enabled by rapid thermal dissipation from a thin micro-LM of a typical size of  $\varnothing 1 \times 10$  mm. However, a  $\varnothing 76.2$  mm OAP can harvest only 4.1 W solar energy even in the relatively high direct solar radiation of  $905 \text{ W/m}^2$  we observed, using the apparatus shown in Fig. 10.14. The improved sunlight-to-laser energy conversion efficiency of 14 % shown in Fig. 10.43, and the thermodynamical limit deduced from a detailed valance theory 31 % [76] gives the output laser power of only 0.6 W and 1.3 W, respectively. For meaningful amount of solar energy utilization, arrays of large numbers of  $\mu$ SPLs should be used.

Mass production and cost-reduction of  $\mu$ SPLs is indeed feasible, as demonstrated by the commercially available “Himawari” solar lighting system composed of compact concentrators and a solar-tracking system [78]. Large-sized solar concentrators with a solar-tracking system and solar-tracking type solar panels cannot be operated on windy days because they suffer from wind forces. Taking this fact into account, a coordinated solar tracking system of an array of compact solar-pumped lasers was designed, as shown in Fig. 10.48 (a). In Fig. 10.48 (a), parallel sliding motion of an upper white panel transmits motions of a single solar-tracking engine to 25  $\mu$ SPLs to realize coordinated solar tracking. The upper white panel is always kept horizontal during its motion to keep the wind pressure minimum. The distances between neighboring  $\mu$ SPLs are determined in the array to avoid spatial interventions between them during the coordinated solar tracking. In the outdoor performance test shown in Fig. 10.48(b), thermal expansion of the upper panel by solar irradiation could disturb precise coordinated tracking. Application of super Invar alloy, whose thermal expansion coefficient between 20 and  $90 \text{ }^\circ\text{C}$  is lower than  $0.1 \times 10^{-6} \text{ K}^{-1}$  (which is as low as 1/100 of that of the popular stainless steel), could overcome this problem. However, application of more cost-effective materials or structures to realize low thermal expansion remains a future challenge [110].

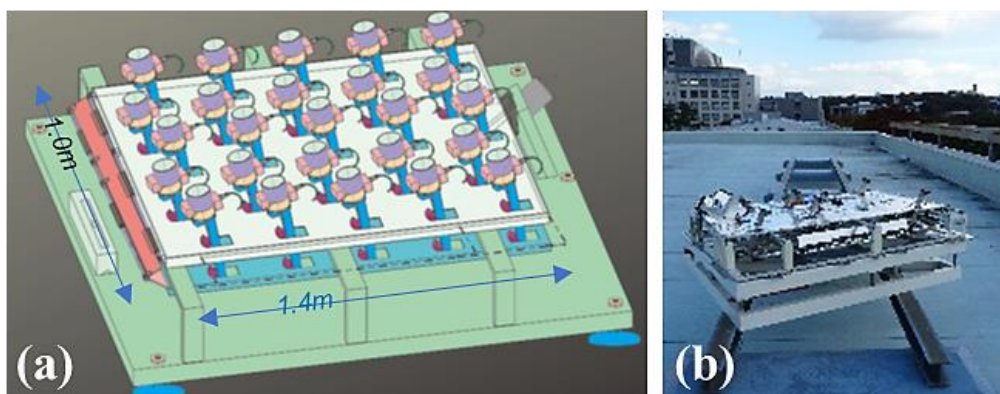


**Fig. 10.48.** (a) Schematic rendering of a coordinated solar tracking system of  $5 \times 5$  compact SPLs and (b) a photograph of outdoor solar tracking operation test.

### 10.11. SPL-PV Combined System and Its Application to Optical Wireless Power Transmission

From the spectral quantum efficiency measured on a Si solar cell of energy conversion efficiency  $\eta = 24.0\%$  [111], the spectral energy conversion efficiency  $\eta(\lambda)$  can be calculated as shown in Fig. 10.49, where  $\lambda$  stands for wavelength [8].  $\eta(\lambda)$  takes a maximum value of over 40% at  $\lambda$  just below the optical absorption band edge of Si = 1117 nm. The solar spectrum, which is also illustrated with its intensity in arbitrary unit for comparison, has a maximum at around 500 nm. Obviously, the solar spectrum does not make a good fit with  $\eta(\lambda)$ . On average in the range of the solar spectrum below 1117 nm,  $\eta$  for crystalline Si solar cells decrease to a level as low as 25-30% as those in the market.

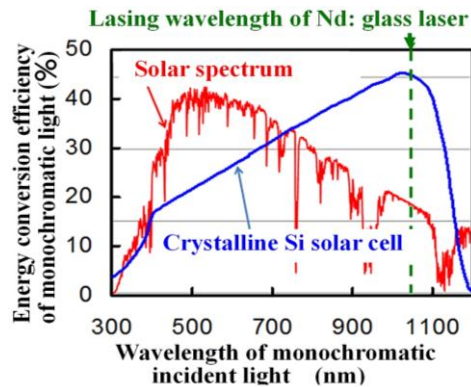


**Fig. 10.49.** Spectral conversion efficiency of a crystalline Si solar cell under monochromatic illumination of around 50 mW/cm<sup>2</sup>. The solar spectrum is also illustrated. The lasing wavelength of the Nd:glass laser is indicated by an arrow.

The residual 70-75% of the solar energy contributes only to the temperature rise of the cell. In contrast, the lasing wavelength of a Nd:glass laser is located just below 1117 nm and closely fits the peak of  $\eta(\lambda)$ . This means that the photon energy can be converted to electricity with minimal heat loss. Therefore, it will be reasonable to convert the output of  $\mu$ SPL into electricity via specially designed Si photovoltaic (PV) cells [10-17].

Optical wireless power transmission [109] to mobile objects may find applications in near future such as power feeding to drones and electric vehicles [4-9]. The extraterrestrial AM0 solar radiation on the Earth's orbit is 1.36 W/m<sup>2</sup>, which is 36% larger than the terrestrial AM1.5 solar radiation. Owing to a lack of interrupters such as clouds, the concept of space solar power stations, on which electricity is generated using solar cells and transmitted to the earth via microwaves or laser beams, has been proposed [1-5]. More recently, electricity generated by solar cells at a lunar lander has been planned for transmission via laser beam to a lunar rover exploring deep into permanently shadowed craters for frozen water [6, 7]. Because all the 1.36 W/m<sup>2</sup> solar radiation in space is direct solar radiation, SPLs can be also applied to generate laser beam for power feeding. The

combined loss of solar energy via energy conversion from sunlight to electricity by solar cells and that from photovoltaic electricity to laser beam by of a laser diode can be higher than the single loss due to conversion from sunlight to laser beam by an SPL [8].

In the terrestrial application of SPLs to laser-beam power feeding, the high concentration ratios of OAPs such as 11550 in Eq. (10.30) and 25990 in Eq. (10.34) exclude the chance to utilize diffuse solar radiation. The reason why the high concentration is requested is to realize high radiation flux density that surpasses  $I_{\text{eth}}$  in Eq. (10.8). According to Eq. (10.8),  $I_{\text{eth}}$  can be lowered if the aspect ratio  $A (= L/r)$  of an LM is large, and the factor  $\alpha$ , the effective utilization rate of the length  $L$  of the LM is large. Disk-shaped LMs such as VECSELs discussed in Section 10.9 and shown as an ideal form of an LM in the top left corner of Fig. 10.6, show good promise in the future. As is also shown in the top right corner of Fig. 10.6, a fiber-type LM is another approach to attain large  $A$  and a large  $\alpha$  by side-pumping in Eq. (10.8). As a promising approach, transverse excitation has been introduced into a solar pumped fiber laser system to decrease the threshold excitation power for oscillation using a low sunlight concentration at the ratio of 1/15 [112-115].

## 10.12. Conclusion

We have developed compact solar-pumped lasers (SPFL and  $\mu$ SPL) employing an off-axis parabolic mirror with an aperture of 50.8 mm or 76.2 mm diameter and a Nd-doped ZBLAN fiber or a Cr-doped Nd (0.1 at%):YAG transparent ceramic rod of  $\varnothing 1 \times 10$  mm as the LM. Here, the stimulated emission takes place via the transition of  $\text{Nd}^{3+}$  in YAG from its excited state to lower energy states. Cr was doped to absorb sunlight in broad wavelength ranges and to transfer the absorbed solar energy to  $\text{Nd}^{3+}$  because  $\text{Nd}^{3+}$  absorbs sunlight only in the limited narrow wavelength ranges. The laser oscillation wavelength of 1.05-1.06  $\mu\text{m}$ , just below the optical absorption edge of Si solar cells, is suitable for photoelectric conversion with minimal thermal loss after optical wireless (laser) power transmission to distant places. The small LMs and solar concentrators realize more stable oscillation by rapid natural air convection cooling and increased mechanical stability during wind exposure in contrast to the conventional large SPLs typically employing a 2 m size solar concentrator. Outdoor operation tracking the Sun yielded continuous oscillation exceeding 6.5 h, considerably improving upon the previously reported 11 min. This shows the applicability of SPLs to whole-day operation and terrestrial and extraterrestrial solar energy utilization.

The measured incident sunlight-to-laser output total energy conversion efficiencies are 0.700.9 %. (slope efficiencies against the input solar power to LMs are 1.15-3.3 %). However, several promising data have been obtained for future improvements. The SPL output increased more than eightfold between an LM with Cr content of 0.0 and that of 0.4 at%. The possibility of 14 % total energy conversion efficiency or more was shown in preliminary experimental and simulated results by the improvement of mode-matching efficiency introducing a refractive index matched core-cladding 3D composite structure into an LM. In contrast, there was evidence of degradation of Cr-codoped Nd:YAG transparent ceramic LMs, possibly by the accumulated sunlight irradiations, and relatively low  $\text{Cr}^{3+}$  to  $\text{Nd}^{3+}$  energy transfer efficiency under broadband sunlight pumping. To

overcome these problems, future studies need to explore novel LMs or to investigate alternative choices of LMs including side-pumped fiber LMs and VECSELs of high spectral and mode-matching efficiency.

## Acknowledgments

This chapter contains research results supported by Advanced Low Carbon Technology Research and Development Program (ALCA), Japan Science and Technology Agency, and Toyota central R&D Laboratories Inc. The authors acknowledge Dr. A. Ikesue for his essential contribution in fabrication of laser mediums. The authors also acknowledge Dr. K. Higuchi, Dr. T. Ito, Dr. T. Kajino, Dr. A. Ichiki, Dr. H. N. Luitel, Dr. D. Inoue, Mr. T. Ichikawa, Mr. Y. Suzuki, Mr. H. Terazawa, Mr. T. Kato, Ms. N. Hara, Mr. K. Watanabe, Mr. S. Takimoto, Mr. D. Kano, Ms. L. T. A. Phuc, Dr. H. Iizuka, Dr. T. Tani, and Dr. M. Umehara for their helpful contributions in this work. The authors also acknowledge Prof. M. Yamaga (Gifu University), and Prof. Y. Ohishi and Assoc. Prof. T. Suzuki (Toyota Technological Institute) for their suggestions and valuable discussions regarding this work. The authors would like to thank Editage ([www.editage.com](http://www.editage.com)) for English language editing. This work was started when all the authors were working for Toyota Central R&D Labs., Inc., Nagakute, Aichi, Japan and was continued after H. Ito and T. Motohiro transferred to Nagoya University, Nagoya, Japan as a collaborative project. K. Hasegawa is now continuing a related research in The Graduate School for the Creation of New Photonics Industries (GPI), Hamamatsu, Shizuoka, Japan.

## References

- [1]. M. Mori, H. Nagayama, Y. Saito, H. Matsumoto, Summary of studies on space solar power systems of the National Space Development Agency of Japan, *Acta Astronaut.*, Vol. 54, 2004, pp. 337-345.
- [2]. I. Cash, CASSIOPEIA – A new paradigm for space solar power, *Acta Astronaut.*, Vol. 159, 2019, pp. 170-178.
- [3]. X. Li, G. Fan, Y. Zhang, X. Ji, M. Li, A Fresnel concentrator with fiber-optic bundle-based space solar power satellite design, *Acta Astronaut.*, Vol. 153, 2018, pp. 122-129.
- [4]. R. J. De Young, Beam profile measurement of a solar-pumped iodine laser, *Appl. Opt.*, Vol. 25, Issue 21, 1986, pp. 3850-3854.
- [5]. S. H. Choi, J. H. Lee, W. E. Meador, E. J. Conway, A 50-kW module power station of directly solar-pumped iodine laser, *J. Sol. Energy Eng. – Transactions of the ASME*, Vol. 119, Issue 4, pp. 304-311.
- [6]. European Space Agency (ESA) Laser-powered Rover to Explore Moon's Dark Shadows, [http://www.esa.int/Enabling\\_Support/Space\\_Engineering\\_Technology/Laser-powered rover to explore Moons' dark shadows](http://www.esa.int/Enabling_Support/Space_Engineering_Technology/Laser-powered_rover_to_explore_Moons'_dark_shadows)
- [7]. W. M. Farrell, T. J. Stubbs, J. S. Halckas, R. M. Killen, G. T. Delory, M. R. Collier, R. R. Vondrak, Anticipated electrical environment within permanently shadowed lunar craters, *J. Geophys. Res.*, Vol. 115, 2010, E03004.
- [8]. T. Motohiro, Y. Takeda, H. Ito, K. Hasegawa, A. Ikesue, T. Ichikawa, K. Higuchi, A. Ichiki, S. Mizuno, T. Ito, N. Yamada, H. N. Luitel, T. Kajino, H. Terazawa, S. Takimoto, K. Watanabe, Concept of the solar-pumped laser-photovoltaics combined system and its

- application to laser beam power feeding to electric vehicles., *Jpn. J. Appl. Phys.*, Vol. 56, 2017, 08MA07.
- [9]. A. Mohammadnia, B. M. Ziapour, H. Ghaebi, M. H. Khooban, Feasibility assessment of next-generation drones powering by laser-based wireless power transfer, *Opt. Laser Technol.*, Vol. 143, 2021, 107283.
- [10]. Y. Takeda, T. Ito, Light trapping for silicon photovoltaic cells illuminated by solar-pumped lasers, *Jpn. J. of Appl. Phys.*, Vol. 54, 2015, 08KD13.
- [11]. Y. Takeda, H. Iizuka, S. Mizuno, K. Hasegawa, T. Ichikawa, H. Ito, T. Kajino, T. Motohiro, Silicon photovoltaic cells coupled with solar-pumped fiber lasers emitting at 1064nm, *J. Appl. Phys.*, Vol. 116, 2014, 014501.
- [12]. Y. Takeda, H. Iizuka, S. Mizuno, K. Hasegawa, T. Ichikawa, H. Ito, T. Kajino, T. Motohiro, Light trapping for emission from a photovoltaic cell under normally incident monochromatic illumination, *J. Appl. Phys.*, Vol. 116, 2014, 124506.
- [13]. Y. Takeda, T. Ito, N. Yamada, K. Hasegawa, S. Mizuno, T. Ichikawa, H. N. Luitel, H. Iizuka, K. Higuchi, H. Ito, A. Ichiki, T. Motohiro, Crystalline silicon photovoltaic cells used for power transmission from solar-pumped lasers: I. Light trapping concepts, *Jpn. J. Appl. Phys.*, Vol. 57, 2018, 08RF05.
- [14]. Y. Takeda, N. Yamada, T. Ito, H. Ito, T. Motohiro, Crystalline silicon photovoltaic cells used for power transmission from solar-pumped lasers: II. Practical implementation, *Jpn. J. Appl. Phys.*, Vol. 57, 2018, 08RF06.
- [15]. N. Yamada, T. Ito, H. Ito, T. Motohiro, Y. Takeda, Crystalline silicon photovoltaic cells used for power transmission from solar-pumped lasers: III. Prototype for proof of the light trapping concept, *Jpn. J. Appl. Phys.*, Vol. 57, 2018, 08RF07.
- [16]. Y. Takeda, Light trapping for photovoltaic cells used for optical power transmission, *Appl. Phys. Express*, Vol. 13, 2020, 054001.
- [17]. Y. Takeda, H. Iizuka, N. Yamada, T. Ito, Light trapping for photovoltaic cells using polarization-insensitive angle-selective filters under monochromatic illumination, *Appl. Opt.*, Vol. 56, Issue 20, 2017, pp. 5761-5767.
- [18]. R. Ishikawa, T. Kato, R. Anzo, M. Nagatake, T. Nishimura, N. Tsuboi, S. Miyajima, Widegap  $\text{CH}_3\text{NH}_3\text{PbBr}_3$  solar cells for optical wireless power transmission application, *Appl. Phys. Lett.*, Vol. 117, 2020, 013902.
- [19]. T. Ohkubo, T. Yabe, K. Yoshida, S. Uchida, T. Funatsu, B. Bagheri, T. Oishi, K. Daito, M. Ishioka, Y. Nakayama, N. Yasunaga, K. Kido, Y. Sato, C. Baasandash, K. Kato, T. Yanagitani, Y. Okamoto, Solar-pumped 80 W laser irradiated by a Fresnel lens, *Opt. Lett.*, Vol. 34, Issue 2, 2009, pp. 175-177.
- [20]. T. Yabe, B. Bagheri, T. Ohkubo, S. Uchida, K. Yoshida, T. Funatsu, T. Oishi, K. Daito, M. Ishioka, N. Yasunaga, Y. Sato, C. Baasandash, Y. Okamoto, K. Yanagitani, 100 W-class solar pumped laser for sustainable magnesium-hydrogen energy cycle, *Jpn. J. Appl. Phys.*, Vol. 104, 2008, 083104.
- [21]. Z. J. Kiss, H. R. Lewis, R. C. Duncan, Sun pumped continuous optical maser, *Appl. Phys. Lett.*, Vol. 2, Issue 5, 1963, pp. 93-94.
- [22]. G. R. Simpson, Continuous sun-pumped room temperature glass laser operation, *Appl. Opt.*, Vol. 3, Issue 6, 1964, pp.783-784.
- [23]. C. G. Young, A sun-pumped CW one-watt laser, *Appl. Opt.*, Vol. 5, 1966, pp. 993-997.
- [24]. T. H. Maiman, Stimulated optical radiation in ruby, *Nature*, Vol. 187, Issue 4736, 1960, pp. 493-494.
- [25]. J. H. Lee, W. R. Weaver, A solar simulator-pumped atomic iodine laser, *Appl. Phys. Lett.*, Vol. 39, 1981, pp. 137-139.
- [26]. C. K. Terry, J. E. Peterson, D. Y. Goswami, Terrestrial solar-pumped iodine gas laser with minimum threshold concentration requirements, *J. Thermophys. Heat Tran.*, Vol. 10, 1996, pp. 54-59.

- [27]. I. M. Belousova, O. B. Danilov, A. A. Mak, V. P. Belousov, V. Y. Zalesslii, V. A. Grigor'ev, A. V. Kris'ko, E. N. Sosnov, Feasibility of the solar-pumped fullerene-oxygen-iodine laser (Sun-Light FOIL), *Optic Spectrosc.*, Vol. 90, 2001, pp. 773-777.
- [28]. I. Pe'er, I. Vishnevitsky, N. Naftali, A. Yogev, Broadband laser amplifier based on gas-phase dimer molecules pumped by the Sun, *Opt. Lett.*, Vol. 26, 2001 pp. 1332-1334.
- [29]. T. Härig, G. Huber, I. A. Schcherbakov, Cr<sup>3+</sup> sensitized Nd<sup>3+</sup>:Li-La-phosphate glass laser, *J. Appl. Phys.*, Vol. 52, 1981, pp. 4450-4452.
- [30]. T. Suzuki, H. Kawai, H. Nasu, M. Hughes, S. Mizuno, K. Hasegawa, H. Ito, Y. Ohishi, Excitation wavelength dependence of quantum efficiencies of Nd-doped glasses for solar pumped fiber lasers, *Proceedings of SPIE*, Vol. 7598, 2010, 75981L.
- [31]. T. Suzuki, H. Kawai, H. Nasu, M. Hughes, S. Mizuno, K. Hasegawa, H. Ito, Y. Ohishi, Quantum efficiency measurements on Nd-doped glasses for solar pumped lasers, *J. Non-Cryst. Solids*, Vol. 356, 2010, pp. 2344-2349.
- [32]. T. Suzuki, H. Nasu, S. Mizuno, H. Ito, K. Hasegawa, Y. Ohishi, Spectroscopic investigation of Nd<sup>3+</sup>-doped ZBLAN glass for solar-pumped lasers, *J. Opt. Soc. Am. B*, Vol. 28, 2011, pp. 2001-2006.
- [33]. T. Suzuki, H. Kawai, H. Nasu, M. Huges, Y. Ohishi, S. Mizuno, H. Ito, K. Hasegawa, Quantum efficiency of Nd<sup>3+</sup>-doped glasses under sunlight excitation, *Opt. Mater.*, Vol. 33, 2011, pp. 1952-1957.
- [34]. S. Mizuno, H. Ito, K. Hasegawa, T. Suzuki, Y. Ohishi, Laser emission from a solar-pumped fiber, *Opt. Express*, Vol. 20, Issue 6, 2012, pp. 5891-5895.
- [35]. Y. Iwata, T. Suzuki, Y. Ohishi, Optical properties of Er<sup>3+</sup>-doped glasses for solar-pumped lasers, *Phys. Status Solidi C*, Vol. 9, Issue. 12, 2012, pp. 2344-2347.
- [36]. R. Reisfeld, Spectroscopic properties of Cr (III) in transparent glass-ceramics and energy transfer from Cr (III) to Nd (III), in B. Jezowska-Trzebiatowska, J. Legendziewicz, W. Stręk (Eds.), in *Proceedings of the 1<sup>st</sup> International School on Excited States of Transition Elements*, World Scientific Publ. Co. Pte Ltd. Singapore, 1989, pp. 440-465.
- [37]. H.-D. Hattendorff, G. Huber, H. G. Danielmeyer, Efficient cross pumping of Nd<sup>3+</sup> by Cr<sup>3+</sup> in Nd (Al, Cr)<sub>3</sub>(BO<sub>3</sub>)<sub>4</sub> lasers, *J. Phys. C Solid State Phys.*, Vol. 11, 1978, pp. 2399-2404.
- [38]. H.-D. Hattendorff, G. Huber, F. Lutz, CW laser action in Nd (Al, Cr)<sub>3</sub> (BO<sub>3</sub>)<sub>4</sub> laser, *Appl. Phys. Lett.*, Vol. 34, 1979, pp. 437-439.
- [39]. D. Pruss, G. Huber, A. Beimowski, V. V. Laptev, I. A. Scherbakov, Y. V. Zharikov, Efficient Cr<sup>3+</sup> sensitized Nd<sup>3+</sup>: GdScGa-Garnet laser at 1.06 μm, *Appl. Phys. B*, Vol. 28, 1982, pp. 355-358.
- [40]. G. A. Thompson, V. Krupkin, A. Yogev, M. Oron, Solar-pumped Nd: Cr: GSGG parallel array laser, *Opt. Eng.*, Vol. 31, 1992, pp. 2644-2646.
- [41]. M. Bass, M. J. Weber, Nd, Cr:YAlO<sub>3</sub> laser tailored for high-efficiency Q-switched operation, *Appl. Phys. Lett.*, Vol. 17, 1970, pp. 395-398.
- [42]. H. Arashi, Y. Oka, N. Sasahara, A. Kaimai, M. Ishigame, A Solar-pumped CW 18 W Nd:YAG Laser, *Jpn. J. Appl. Phys.*, Vol. 23, 1984, pp. 1051-1053.
- [43]. M. Weksler, J. Schwartz, Solar-pumped solid-state lasers, *IEEE J. Quant. Electron.*, Vol. 24, 1988, pp. 1222-1228.
- [44]. D. Cooke, Sun-pumped lasers: revisiting an old problem with nonimaging optics, *Appl. Opt.*, Vol. 31, Issue 36, 1992, pp. 7541-7546.
- [45]. A. Ikesue, Y. L. Aung, Ceramic laser materials, *Nat. Photonics*, Vol. 2, 2008, 721.
- [46]. A. Ikesue, Y. L. Aung, V. Lupei, Ceramic Lasers, *Cambridge University Press*, 2013.
- [47]. T. Saiki, S. Motokoshi, K. Imasaki, K. Fujioka, H. Fujita, M. Nakatsuka, Y. Izawa, C. Yamanaka, Effective fluorescence lifetime and stimulated emission cross section of Nd/Cr:YAG ceramics under CW lamplight pumping, *Jpn. J. Appl. Phys.*, Vol. 47, Issue 10, 2008, pp. 7896-7902.

- [48]. R. M. J. Benmair, J. Kagan, Y. Kalisky, Y. Noter, M. Oron, Y. Shimony, A. Yogev, Solar-pumped Er, Tm, Ho:YAG laser, *Opt. Lett.*, Vol. 15, 1990, pp. 36-38.
- [49]. G. A. Thompson, A. Yogev, A. Reich, M. Oron, Effects of coolant temperature and pump power on the power output of solar-pumped solid-state lasers, *Opt. Eng.*, Vol. 31, 1992, pp. 2488-2491.
- [50]. I. L. Pe'er, N. Naftali, D. Abramovic, A. Yogev, M. Lando, Y. Shimony, Passive Q-switching of high-power solar-pumped Nd:YAG laser, *Proceeding of SPIE*, Vol. 3092, 1997, pp. 273-276.
- [51]. I. Pe'er, N. Naftali, A. Yogev, High power, solar pumped, Nd:YAG laser amplifier for free space laser communication, *Proceeding of SPIE*, Vol. 3139, 1997, pp. 194-204.
- [52]. N. Naftali, I. Pe'er, A. Yogev, Power transmission using solar pumped laser, *Proceeding of SPIE*, Vol. 3139, 1997, pp. 259-265.
- [53]. M. Lando, Y. Shimony, R. M. J. Benmair, D. Abramovich, V. Krupkin, A. Yogev, Visible solar-pumped lasers, *Opt. Mater.*, Vol. 13, 1999, pp. 111-115.
- [54]. M. Lando, Y. Shimony, Y. Noter, R. M. J. Benmair, A. Yogev, Passive Q switching of a solar-pumped Nd:YAG laser, *Appl. Opt.*, Vol. 39, 2000, pp. 1962-1965.
- [55]. M. Lando, J. Kagan, B. Linyokin, V. Dobrusin, A solar-pumped Nd:YAG laser in the high collection efficiency regime, *Optic Commun.*, Vol. 222, 2003, pp. 371-381.
- [56]. S. Payziyev, K. Makhmudov, Solar pumped Nd:YAG laser efficiency enhancement using Cr: LiCAF frequency down-shifter, *Optic Commun.*, Vol. 380, 2016, pp. 57-60.
- [57]. J. Almeida, D. Liang, C. R. Vistas, R. Bouadjemine, E. Guillot, 5.5 W continuous wave TEM<sub>00</sub>-mode Nd:YAG solar laser by a light-guide/2 V shaped pump cavity, *Appl. Phys. B Laser Optic.*, Vol. 121, 2015, pp. 473-482.
- [58]. D. Liang, J. Almeida, C. R. Vistas, E. Guillot, Solar-pumped Nd:YAG laser with 31.5 W/m<sup>2</sup> multimode and 7.9 W/m<sup>2</sup> TEM<sub>00</sub>-mode collection efficiencies, *Sol. Energy Mater. Sol. Cells*, Vol. 159, 2017, pp. 435-439.
- [59]. D. Liang, C. R. Vistas, J. Almeida, B. D. Tibúrcio, D. Garcia, Side-pumped continuous-wave Nd:YAG solar laser with 5.4 % slope efficiency, *Sol. Energy Mater. Sol. Cells*, Vol. 192, 2019, pp. 147-153.
- [60]. D. Liang, C. R. Vistas, B. D. Tibúrcio, J. Almeida, Solar-pumped Cr:Nd:YAG ceramic laser with 6.7 % slope efficiency, *Sol. Energy Mater. Sol. Cells*, Vol. 185, 2018, pp. 75-79.
- [61]. P. Xu, S. Yang, C. Zhao, Z. Guan, H. Wang, Y. Zhang, H. Zhang, T. He, High efficiency solar-pumped laser with a grooved Nd:YAG rod, *Appl. Opt.*, Vol. 53, Issue 18, 2014, pp. 3941-3944.
- [62]. T. H. Dinh, T. Ohkubo, T. Yabe, Development of solar concentrators for high-power solar-pumped lasers, *Appl. Opt.*, Vol. 53, 2014, pp. 2711-2719.
- [63]. D. Liang, J. Almeida, Solar-pumped TEM<sub>00</sub> mode Nd:YAG laser, *Opt. Express*, Vol. 21, Issue 21, 2013, pp. 25107-25112.
- [64]. T. Yabe, T. Ohkubo, S. Uchida, K. Yoshida, M. Nakatsuka, T. Funatsu, A. Mabuti, A. Oyama, K. Nakagawa, T. Oishi, K. Daito, B. Behgol, Y. Nakayama, M. Yoshida, S. Motokoshi, Y. Sato, C. Baasandash, High-efficiency and economical solar-energy-pumped laser with Fresnel lens and chromium codoped laser medium, *Appl. Phys. Lett.*, Vol. 90, Issue 26, 2007, 261120.
- [65]. D. Liang, J. Almeida, C. R. Vistas, 25 W/m<sup>2</sup> collection efficiency solar-pumped Nd:YAG laser by a heliostat-parabolic mirror system, *Appl. Opt.*, Vol. 55, Issue 27, 2016, pp. 7712-7717.
- [66]. H. N. Luitel, S. Mizuno, T. Tani, Y. Takeda, Broadband-sensitized upconversion of ATiO<sub>3</sub>:Er,Ni (A = Mg, Ca, Sr, Ba), *J. Ceram. Soc. Jpn*, Vol. 125, Issue 11, 2017, pp. 821-828.

- [67]. Y. Takeda, H. N. Luitel, S. Mizuno, Competing effects of sensitization and energy dissipation by  $\text{Ni}^{2+}$  incorporation in  $\text{La}(\text{Ga}_{0.5}\text{Sc}_{0.5})\text{O}_3:\text{Er}, \text{Ni}, \text{Nb}$  upconverters, *J. Lumin.*, Vol. 194, 2018, pp. 778-784.
- [68]. H. N. Luitel, S. Mizuno, T. Nonaka, T. Tani, Y. Takeda, Effect of Ti compositions for efficiency enhancement of  $\text{CaTiO}_3:\text{Er}^{3+}, \text{Ni}^{2+}$  broadband-sensitive upconverter, *RSC Adv.*, Vol. 7, Issue 66, 2017, pp. 41311-41320.
- [69]. H. N. Luitel, S. Mizuno, Y. Takeda,  $\text{CaTiO}_3:\text{Er}^{3+}, \text{Ni}^{2+}$  broadband-sensitive upconverter: An effective way to harvest unused NIR solar irradiation for crystalline silicon solar cells, *Phys. Status Solidi*, Vol. 214, Issue 8, 2017, 1600899.
- [70]. Y. Takeda, S. Mizuno, H. N. Luitel, T. Tani, Broadband-sensitive upconverters co-doped with  $\text{Er}^{3+}$  and  $\text{Ni}^{2+}$  for crystalline silicon solar cells, *Proceeding of SPIE*, Vol. 9937, 2016, 99370E.
- [71]. H. N. Luitel, S. Mizuno, Y. Takeda, Effect of A-sites cations on the broadband sensitive upconversion of  $\text{AZrO}_3:\text{Er}, \text{Ni}$  (A = Mg, Ca, Sr, Ba) phosphors, *Opt. Mater.*, Vol. 64, 2017, pp. 314-322.
- [72]. Y. Takeda, S. Mizuno, H. N. Luitel, K. Yamanaka, Broadband-sensitive cooperative upconversion emission of  $\text{La}(\text{Ga}_{0.5}\text{Sc}_{0.5})\text{O}_3:\text{Er}, \text{Ni}, \text{Nb}$ , *Appl. Phys. Express*, Vol. 9, Issue 11, 2016, 112402.
- [73]. Y. Takeda, S. Mizuno, H. N. Luitel, K. Yamanaka, T. Tani, Energy transfer between  $\text{Ni}^{2+}$  sensitizers and  $\text{Er}^{3+}$  emitters in broadband-sensitive upconverters  $\text{La}(\text{Ga}, \text{Sc}, \text{In})\text{O}_3:\text{Er}, \text{Ni}, \text{Nb}$ , *J. Appl. Phys.* Vol. 120, Issue 7, 2016, 073102.
- [74]. H. N. Luitel, S. Mizuno, T. Tani, Y. Takeda, Broadband sensitive  $\text{Ni}^{2+}\text{-Er}^{3+}$  based upconverters for crystalline silicon solar cells, *RSC Adv.*, Vol. 6, Issue 60, 2016, pp. 55499-55506.
- [75]. Y. Takeda, S. Mizuno, H. N. Luitel, T. Tani, A broadband-sensitive upconverter  $\text{La}(\text{Ga}_{0.5}\text{Sc}_{0.5})\text{O}_3:\text{Er}, \text{Ni}, \text{Nb}$  for crystalline silicon solar cells, *Appl. Phys. Lett.*, Vol. 108, 2016, 043901.
- [76]. S. Nechayev, C. Rotschild, Detailed balance limit of efficiency of broadband-pumped lasers, *Sci. Rep.*, Vol. 7, 2017, 11497.
- [77]. F. A. Jenkins, H. E. White, Fundamentals of Optics, 3<sup>rd</sup> Ed., *McGraw-Hill Kogakusha Ltd.*, 1957.
- [78]. Himawari Solar Lighting System La Foret Engineering Co. Ltd., [https://www.himawari-net.co.jp/e\\_page-index01.html](https://www.himawari-net.co.jp/e_page-index01.html)
- [79]. R. E. Bird, C. Riordan, Simple solar spectral model for direct and diffuse irradiance on horizontal and tilted planes at the earth's surface for cloudless atmospheres, *J. Appl. Meteorol. Climatol.*, Vol. 25, Issue 1, 1986, pp. 87-97.
- [80]. T. Suzuki, H. Nasu, M. Hughes, S. Mizuno, K. Hasegawa, H. Ito, Y. Ohishi, Quantum efficiency measurements on Nd-doped glasses for solar pumped lasers, *J. Non-Cryst. Solids*, Vol. 356, Issues 44-49, 2010, pp. 2344-2349.
- [81]. S. E. Stokowski, R. A. Saroyan, M. J. Weber, Nd-doped Laser Glass Spectroscopic and Physical Properties, Tech. Rep. 1, *Lawrence Livermore National Laboratory*, 1981.
- [82]. S. E. Stokowski, R. A. Saroyan, M. J. Weber, Nd-doped Laser Glass Spectroscopic and Physical Properties, Tech. Rep. 2, *Lawrence Livermore National Laboratory*, 1981.
- [83]. H. Toratani, T. Izumitani, H. Kuroda, Compositional dependence of nonradiative decay rate in Nd laser glasses, *J. Non-Cryst. Solids*, Vol. 52, Issues 1-3, 1982, pp. 303-313.
- [84]. I. Bardez, D. Caurant, J. L. Dussossoy, P. Loiseau, C. Gervais, F. Ribot, D. R. Neuville, N. Baffier, C. Fillett, Development and characterization of rare earth-rich glassy matrices envisaged for the immobilization of concentrated nuclear waste solutions, *Nucl. Sci. Eng.*, Vol. 153, Issue 3, 2006, pp. 272-284.
- [85]. M. Poulain, M. Poulain, J. Lucas, Verres fluores au tetrafluorure de zirconium proprietes optiques d'un verre dope au  $\text{Nd}^{3+}$ , *Mat. Res. Bull.*, Vol. 10, Issue 4, 1975, pp. 243-246.

- [86]. T. Kanamori, S. Sakaguchi, Preparation of elevated NA fluoride optical fibers, *Jpn. J. Appl. Phys.*, Vol. 25, Issue 6A, 1986, pp. L468-L470.
- [87]. F. Gan, Optical properties of fluoride glasses: A review, *J. Non-Cryst. Solids.*, Vol. 184, 1995, pp. 9-20.
- [88]. K. Arai, H. Namikawa, K. Kumata, T. Honda, Y. Ishii, T. Hanada, Aluminum or phosphorus co-doping effects on the fluorescence and structural properties of neodymium-doped silica glass, *J. Appl. Phys.*, Vol. 59, Issue 10, 1986, pp. 3430-3436.
- [89]. J. Heber, Solar fibre lasers, *Nature Materials*, Vol. 11, 2012, 266.
- [90]. Z. J. Kiss, R. C. Duncan, Cross-pumped  $\text{Cr}^{3+}$ - $\text{Nd}^{3+}$ : YAG laser system, *Appl. Phys. Lett.*, Vol. 5, Issue 10, 1964, pp. 200-201.
- [91]. T. H. Dinh, T. Ohkubo, T. Yabe, H. Kuboyama, 120-watt continuous wave solar-pumped laser with a liquid light-guide lens and an Nd: YAG rod, *Opt. Lett.*, Vol. 37, Issue 3, 2012, pp. 2670-2672.
- [92]. T. Saiki, N. Fujiwara, N. Matsuoka, M. Nakatuka, K. Fujioka, Y. Iiida, Amplification properties of KW Nd/Cr:YAG ceramic multi-stage active-mirror laser using white-light pump source at high temperatures, *Opt. Commun.*, Vol. 387, 2017, pp. 316-321.
- [93]. M. Endo, Feasibility study of a conical-toroidal mirror resonator for solar-pumped thin-disk lasers, *Opt. Express*, Vol. 15, Issue 9, 2007, pp. 5482-5493.
- [94]. T. Ogawa, S. Wada, M. Higuchi, Development of Nd, Cr co-doped laser materials for solar-pumped lasers, *Jpn. J. Appl. Phys.*, Vol. 53, 2014, 08MG03.
- [95]. Y. Honda, S. Motokoshi, T. Jitsuno, N. Miyana, K. Fujioka, M. Nakatsuka, M. Yoshida, Temperature dependence of optical properties in Nd/Cr: YAG materials, *J. Lumin.*, Vol. 148, 2014, pp. 342-346.
- [96]. M. Yamaga, Y. Oda, H. Uno, K. Hasegawa, H. Ito, S. Mizuno, Formation probability of Cr-Nd pair and energy transfer from Cr to Nd in  $\text{Y}_3\text{Al}_5\text{O}_{12}$  ceramics codoped with Nd and Cr, *J. Appl. Phys.*, Vol. 112, 2012, 063508.
- [97]. K. Hasegawa, T. Ichikawa, S. Mizuno, Y. Takeda, H. Ito, A. Ikesue, T. Motohiro, M. Yamaga, Energy transfer efficiency from  $\text{Cr}^{3+}$  to  $\text{Nd}^{3+}$  in solar-pumped laser using transparent Nd/Cr:  $\text{Y}_3\text{Al}_5\text{O}_{12}$  ceramics, *Opt. Express*, Vol. 23, Issue 11, 2015, pp. A519-A524.
- [98]. W. Koechner, Solid-State Laser Engineering, 5<sup>th</sup> Ed., *Springer-Verlag*, Berlin, 2003.
- [99]. S. Mehellou, D. Liang, J. Almeida, R. Bouadjemine, C. R. Vistas, E. Guillot, F. Rehouma, Stable solar-pumped TEM<sub>00</sub>-mode 1064 nm laser emission by a monolithic fused silica twisted light guide, *Sol. Energy*, Vol. 155, 2017, pp. 1059-1071.
- [100]. Y. Suzuki, H. Ito, T. Kato, L.T.A. Phuc, K. Watanabe, H. Terazawa, K. Hasegawa, T. Ichikawa, S. Mizuno, A. Ichiki, S. Takimoto, A. Ikesue, Y. Takeda, T. Motohiro, Continuous oscillation of a compact solar-pumped Cr, Nd-doped YAG ceramic rod laser for more than 6.5 h tracking the sun, *Sol. Energy*, Vol. 177, 2019, pp. 440-447.
- [101]. T. Kato, H. Ito, K. Hasegawa, T. Ichikawa, A. Ikesue, S. Mizuno, Y. Takeda, A. Ichiki, T. Motohiro, Effect of Cr content on the output of a solar-pumped laser employing a Cr-doped Nd: YAG ceramic laser medium operating in sunlight, *Jpn. J. Appl. Phys.*, Vol. 58, 2019, 062007.
- [102]. D. Findlay, R. Clay, The measurement of internal losses in 4-level lasers, *Phys. Lett.*, Vol. 20, Issue 3, 1966, pp. 277-278.
- [103]. K. Hasegawa, T. Ichikawa, Y. Takeda, A. Ikesue, H. Ito, T. Motohiro, Lasing characteristics of refractive-index-matched composite  $\text{Y}_3\text{Al}_5\text{O}_{12}$  rods employing transparent ceramics for solar-pumped lasers, *Jpn. J. Appl. Phys.*, Vol. 57, 2018, 042701.
- [104]. T. Kato, H. Ito, K. Hasegawa, T. Ichikawa, A. Ikesue, S. Mizuno, Y. Takeda, A. Ichiki, T. Motohiro, Energy transfer efficiency from  $\text{Cr}^{3+}$  to  $\text{Nd}^{3+}$  in Cr, Nd YAG ceramics laser media in a solar-pumped laser in operation outdoors, *Opt. Mater.*, Vol. 110, 2020, 110481.

- [105]. K. Takagi, M. Yamaga, E. G. Villora, K. Shimamura, K. Hasegawa, H. Ito, S. Mizuno, Y. Takeda, T. P. J. Han, Energy transfer from Cr to Nd in substitutional crystal  $Y_3Ga_xAl_{5-x}O_{12}$  codoped with Nd and Cr, *J. Lumin.*, Vol. 169, 2016, pp. 65-71.
- [106]. M. Yamaga, T. P. J. Han, O. Sawada, E.G. Villorac, K. Shimamura, K. Hasegawa, S. Mizuno, Y. Takeda, Laser oscillation of Nd via energy transfer process from Cr to Nd in substitutional disordered garnet crystals codoped with Nd and Cr, *J. Lumin.*, Vol. 202, 2018, pp. 393-402.
- [107]. A. H. Quarterman, K. G. Wilcox, Design of a solar-pumped semiconductor laser, *Optica*, Vol. 2, Issue 1, 2015, pp. 56-61.
- [108]. S. Unnikrishnan, N. G. Anderson, Quantum-well lasers for direct solar photo pumping, *J. Appl. Phys.*, Vol. 74, Issue 6, 1993, pp. 4221-4228.
- [109]. T. Miyamoto, Optical wireless power transmission using VECSELs, *Proceedings of SPIE*, Vol. 10682, 2018, 1068204.
- [110]. T. Motohiro, A. Ichiki, T. Ichikawa, H. Ito, K. Hasegawa, S. Mizuno, T. Ito, T. Kajino, Y. Takeda, K. Higuchi, Consideration of coordinated solar tracking of an array of compact solar-pumped lasers combined with photovoltaic cells for electricity generation, *Jpn. J. Appl. Phys.*, Vol. 54, 2015, 08KE04.
- [111]. J. Zhao, A. Wang, P. P. Altermatt, S. R. Wenham, M. A. Green, 24 % efficient per silicon solar cell: Recent improvements in high efficiency silicon cell research, *Sol. Energy Mater. Sol. Cells*, Vols. 41-42, 1996, pp. 87-99.
- [112]. T. Masuda, M. Iyoda, Y. Yasumatsu, M. Endo, Low-concentrated solar pumped laser via transverse excitation fiber-laser geometry, *Opt. Lett.*, Vol. 42, Issue 17, 2017, pp. 3427-3430.
- [113]. M. Endo, J.-F. Bisson, T. Masuda, Monte Carlo simulation of a transversely excited solar-pumped fiber laser, *Jpn. J. Appl. Phys.*, Vol. 58, 2019, 112006.
- [114]. T. Masuda, Y. Zhang, C. Ding, F. Liu, K. Sasaki, Q. Shen, M. Endo, All-inorganic cesium lead halide perovskite nanocrystals for solar-pumped laser application, *J. Appl. Phys.*, Vol. 127, 2020, 243104.
- [115]. T. Masuda, M. Iyoda, Y. Yasumatsu, S. Dottermusch, I. A. Howard, B. S. Richards, J.-F. Bisson, M. Endo, A fully planar solar pumped laser based on a luminescent solar collector, *Commun. Phys.*, Vol. 3, 2020, pp.1-6.